

Modeling fractures as interfaces with nonmatching grids

Najla Frih · Vincent Martin · Jean Elizabeth Roberts ·
Ali Saâda

Received: 2 February 2011 / Accepted: 4 June 2012 / Published online: 25 July 2012
© Springer Science+Business Media B.V. 2012

Abstract We consider a model for fluid flow in a porous medium with a fracture. In this model, the fracture is treated as an interface between subdomains, on which specific equations have to be solved. In this article, we analyze the discrete problem, assuming that the fracture mesh and the subdomain meshes are completely independent, but that the geometry of the fracture is respected. We show that despite this nonconformity, first-order convergence is preserved with the lowest-order Raviart–Thomas(-Nedelec) mixed finite elements. Numerical simulations confirm this result.

Keywords Fractures · Barriers · Mixed finite elements · Flow in porous media · Nonmatching grids · Nonconforming meshes

Mathematics Subject Classifications (2010) 76S05 · 35Q86 · 65M60

N. Frih · A. Saâda
ENIT-LAMSIN, BP 37, 1002 Tunis-le Belvédère, Tunisia

N. Frih
e-mail: najla.frih@lamsin.rnu.tn

A. Saâda
e-mail: ali.saada@ipein.rnu.tn

V. Martin
LMAC, UTC, Royallieu, BP 20 529,
60 205 Compiègne CEDEX, France
e-mail: vincent.martin@utc.fr

J. E. Roberts (✉) · V. Martin
INRIA-Paris Rocquencourt, BP 105,
78153 Le Chesnay CEDEX, France
e-mail: jean.roberts@inria.fr

1 Introduction

The modeling of flow in porous media with large fractures is important for many engineering applications such as petroleum reservoir modeling or nuclear waste storage monitoring. It has long been an important area of research. We are particularly interested in discrete fracture models, in which there is communication between the matrix and the fracture. In [2, 3, 10, 15] and in [17], models for flow in fractured porous media were introduced. These were models in which the fractures were treated individually, and they were identified as $(n - 1)$ -dimensional interfaces in the n -dimensional domain. These models were analyzed and numerical results, obtained with a mixed finite element discretization, were given. The models were presented as domain decomposition techniques with nonlocal interface conditions on the interface between the subdomains; however, it was assumed that a finite element grid for the entire domain was used and that the fracture coincided with a union of faces of elements of the discretization grid. In [11, 12] and in (Knabner and Roberts 2012, submitted), this model was extended to a model in which the flow in the fracture was governed by Forchheimer's law while that in the rest of the domain was governed by Darcy's law, and in [12], it was observed that the results were still correct if completely independent grids were used for the subdomains on either side of a fracture and for the fracture itself. The object of this article is to give a demonstration of the existence and uniqueness of the solution when nonmatching grids are used for the model of [15, 17], which generalizes the model of [2, 3] to include the case of fractures of low permeability and to show that optimal order convergence is maintained when the Raviart–Thomas–Nedelec elements of low-

est order are used. It is interesting to point out that, contrary to what is obtained for the mortar method [6, 7], no restrictions on the mesh size of the interface are necessary to obtain optimal order convergence; in particular, one can use a mesh that is very fine in the fracture. We also carry out a numerical study to corroborate these theoretical results.

We remark that in this article, we have restricted our attention to the simplest model in which a domain is divided into two disjoint subdomains by a simple fracture, and Darcy flow is considered throughout the domain and fracture. However, similar fracture models for more complex situations have been studied; e.g., a simple network of fractures cf. [4], Forchheimer flow in the fractures [11, 12] and (Knabner and Roberts 2012, submitted), Darcy–Brinkman flow in the fractures [16], embedded fractures [5, 18], multiphase flow [19], and for the models of [4] and [11, 12] (Knabner and Roberts 2012, submitted), good numerical results have been obtained with nonmatching grids.

We also remark that although we use nonmatching meshes in the subdomains and in the fracture, we do require that the geometry of the fracture is respected by the meshes. In [9], a formulation based on enriched finite elements allows the meshing of the entire domain independently of the fracture, for a case in which there is no flow along the fracture. Recently, in [14], a formulation also using enriched finite elements was introduced for fracture treatment; in [21], a fracture model using two interfaces for one single fracture is proposed for handling nonmatching grids.

2 Description of the problem

Suppose that Ω is a convex domain in \mathbb{R}^n , $n = 2$, or 3 and denote by $\Gamma = \partial\Omega$ the boundary of Ω . We consider single phase, incompressible flow in Ω , and for simplicity, we neglect gravitational effects. We suppose that the flow in Ω is governed by the conservation equation together with Darcy's law relating the gradient of the pressure p to the Darcy velocity \mathbf{u} :

$$\begin{aligned} \operatorname{div} \mathbf{u} &= g & \text{in } \Omega \\ \mathbf{u} &= -\mathbf{K} \nabla p & \text{in } \Omega \\ p &= \bar{p} & \text{on } \Gamma, \end{aligned} \quad (1)$$

where p is the pressure, \mathbf{u} is the Darcy velocity, \mathbf{K} is the hydraulic conductivity (or permeability) tensor, f is a source term, and \bar{p} is the given pressure on the boundary Γ . We suppose that \mathbf{K} is symmetric, bounded, and uniformly positive definite.

For simplicity, for the model problem considered here, it is supposed that the fracture, Ω_f , is a subdomain of Ω , that there is a hyperplane γ and a unit vector $\mathbf{n} = \mathbf{n}_1 = -\mathbf{n}_2$ normal to γ such that

$$\begin{aligned} \Omega_f &= \left\{ \mathbf{x} = \mathbf{s} + \sigma \mathbf{n} \in \Omega : \mathbf{s} \in \gamma, \right. \\ &\quad \left. \text{and } \sigma \in \left(-\frac{d(\mathbf{s})}{2}, \frac{d(\mathbf{s})}{2} \right) \right\}, \end{aligned}$$

where $d(\mathbf{s})$ denotes the thickness of the fracture at $\mathbf{s} \in \gamma$. It is also supposed that the width function d on γ is bounded above and below by positive constants.

It is further assumed that Ω_f separates Ω into two connected subdomains:

$$\Omega \setminus \overline{\Omega_f} = \Omega_1 \cup \Omega_2, \quad \Omega_1 \cap \Omega_2 = \emptyset.$$

Let $\Gamma_i = \partial\Omega_i \cap \Gamma$ be the part of the boundary of Ω_i in common with the boundary of Ω , $i = 1, 2, f$, and let $\gamma_i = \partial\Omega_i \cap \partial\Omega_f \cap \Omega$ be the part of the boundary of Ω_i in common with the boundary of the fracture Ω_f , $i = 1, 2$. Let \mathbf{n}_i be the outward unit normal vector field on Ω_i , $i = 1, 2, f$.

If we denote by p_i , \mathbf{u}_i , \mathbf{K}_i , and q_i , the restrictions of p , \mathbf{u} , \mathbf{K} , and q , respectively, to Ω_i , $i = 1, 2, f$, and by \bar{p}_i the restriction of \bar{p} to Γ_i , $i = 1, 2, f$, then problem (1) is clearly equivalent to the following transmission problem:

$$\begin{aligned} \operatorname{div} \mathbf{u}_i &= g_i & \text{in } \Omega_i, i = 1, 2, f, \\ \mathbf{u}_i &= -\mathbf{K}_i \nabla p_i & \text{in } \Omega_i, i = 1, 2, f, \\ p_i &= \bar{p}_i & \text{on } \Gamma_i, i = 1, 2, f, \\ p_i &= p_f & \text{on } \gamma_i, i = 1, 2, \\ \mathbf{u}_i \cdot \mathbf{n} &= \mathbf{u}_f \cdot \mathbf{n} & \text{on } \gamma_i, i = 1, 2. \end{aligned} \quad (2)$$

The model problem with the fracture reduced to the interface γ is obtained by averaging across the fracture the first three equations of Eq. 2 for the index f . Using the notation ∇_τ (respectively div_τ) for the tangential gradient (respectively the tangential divergence) operator along the fracture γ and denoting by p_γ and \mathbf{u}_γ the pressure and the (tangential) velocity on the fracture interface γ , we obtain the following interface problem:

$$\begin{aligned} \mathbf{u}_i &= -\mathbf{K}_i \nabla p_i & \text{in } \Omega_i \\ \operatorname{div} \mathbf{u}_i &= g_i & \text{in } \Omega_i \\ \mathbf{u}_\gamma &= -\mathbf{K}_\gamma \nabla_\tau p_\gamma & \text{in } \gamma \\ \operatorname{div}_\tau \mathbf{u}_\gamma &= g_\gamma + (\mathbf{u}_1 \cdot \mathbf{n}_1|_\gamma + \mathbf{u}_2 \cdot \mathbf{n}_2|_\gamma) & \text{in } \gamma \\ \kappa_\gamma (p_i - p_\gamma) &= \xi \mathbf{u}_i \cdot \mathbf{n}_i - \bar{\xi} \mathbf{u}_{i+1} \cdot \mathbf{n}_{i+1} & \text{in } \gamma \\ p_i &= \bar{p}_i & \text{on } \Gamma_i \\ p_\gamma &= \bar{p}_\gamma & \text{on } \partial\gamma, \end{aligned} \quad (3)$$

where we have supposed that the index $i = 1, 2$ belongs to $Z_2 = Z/[2]$ so that $2 + 1 = 1$, and we have assumed that \mathbf{K}_f is composed of a tangential part $\mathbf{K}_{f,\tau}$ and a normal part $\mathbf{K}_{f,v}$ and where $\mathbf{K}_\gamma = \mathbf{K}_{f,\tau}d$ is the tangential permeability $\mathbf{K}_{f,\tau}$ times the width d , $\kappa_\gamma = 2\mathbf{K}_{f,v}/d$ is the normal permeability $\mathbf{K}_{f,v}$ divided by half the fracture width, \bar{p}_γ is the average across the fracture of \bar{p}_f , and g_γ is the integral across the fracture of the source term g_f , ξ is a parameter with $\xi > \frac{1}{2}$ and $\bar{\xi} = 1 - \xi$. The new unknown functions p_γ and \mathbf{u}_γ represent the average pressure across the fracture and the total flux of \mathbf{u}_f across a cross section of the fracture Ω_f . The fifth equation of Eq. 3 is derived by averaging the normal component in Darcy's law across the fracture and using a quadrature rule with weights ξ and $\bar{\xi}$ in the quadrature rule for integrating $\mathbf{u}_f \cdot \mathbf{n}$ across the fracture (see [17]).

3 Weak formulation of the model problem

The weak formulation of Eq. 3 is defined with the Hilbert spaces M and \mathbf{W} :

$$M = L^2(\Omega_1) \times L^2(\Omega_2) \times L^2(\gamma)$$

$$\mathbf{W} = \{\mathbf{v} = (\mathbf{v}_1, \mathbf{v}_2, \mathbf{v}_\gamma) \in H(\text{div}, \Omega_1) \times H(\text{div}, \Omega_2) \times H(\text{div}_\tau, \gamma),$$

$$\text{with } \mathbf{v}_i \cdot \mathbf{n} \in L^2(\gamma), i = 1, 2\},$$

which are equipped with the norms, for an $r = (r_1, r_2, r_\gamma) \in M$ and a $\mathbf{v} = (\mathbf{v}_1, \mathbf{v}_2, \mathbf{v}_\gamma) \in \mathbf{W}$,

$$\|r\|_M^2 = \sum_{i=1}^2 \|r_i\|_{0,\Omega_i}^2 + \|r_\gamma\|_{0,\gamma}^2,$$

$$\|\mathbf{v}\|_{\mathbf{W}}^2 = \sum_{i=1}^2 (\|\mathbf{v}_i\|_{0,\Omega_i}^2 + \|\text{div } \mathbf{v}_i\|_{0,\Omega_i}^2) + \|\mathbf{v}_\gamma\|_{0,\gamma}^2$$

$$+ \|\text{div}_\tau \mathbf{v}_\gamma\|_{0,\gamma}^2 + \sum_{i=1}^2 \|\mathbf{v}_i \cdot \mathbf{n}\|_{0,\gamma}^2.$$

Let the bilinear forms $a : \mathbf{W} \times \mathbf{W} \rightarrow \mathbb{R}$ and $b : \mathbf{W} \times M \rightarrow \mathbb{R}$ be defined by

$$a(\mathbf{u}, \mathbf{v}) = \sum_{i=1}^2 (\mathbf{K}_i^{-1} \mathbf{u}_i, \mathbf{v}_i)_{\Omega_i} + (\mathbf{K}_\gamma^{-1} \mathbf{u}_\gamma, \mathbf{v}_\gamma)_\gamma \\ + \sum_{i=1}^2 (\kappa_\gamma^{-1} (\xi \mathbf{u}_i \cdot \mathbf{n} + \bar{\xi} \mathbf{u}_{i+1} \cdot \mathbf{n}), \mathbf{v}_i \cdot \mathbf{n})_\gamma$$

$$b(\mathbf{u}, r) = \sum_{i=1}^2 (\text{div } \mathbf{u}_i, r_i)_{\Omega_i} + (\text{div}_\tau \mathbf{u}_\gamma, r_\gamma)_\gamma \\ - ([\mathbf{u} \cdot \mathbf{n}], r_\gamma)_\gamma,$$

where we have used the notation

$$[\mathbf{u} \cdot \mathbf{n}] = \mathbf{u}_1 \cdot \mathbf{n} - \mathbf{u}_2 \cdot \mathbf{n} = \mathbf{u}_1 \cdot \mathbf{n}_1 + \mathbf{u}_2 \cdot \mathbf{n}_2 \quad \text{on } \gamma,$$

and let the linear forms $L_q : M \rightarrow \mathbb{R}$ and $L_d : \mathbf{W} \rightarrow \mathbb{R}$ be those associated with the source term and with the Dirichlet data, respectively:

$$L_q(r) = \sum_{i=1}^2 (q_i, r_i)_{\Omega_i} + (q_\gamma, r_\gamma)_\gamma,$$

$$L_d(\mathbf{v}) = - \sum_{i=1}^2 (\mathbf{v}_i \cdot \mathbf{n}_i, \bar{p}_i)_{\Gamma_i} - (\mathbf{v}_\gamma \cdot \mathbf{n}_\gamma, \bar{p}_\gamma)_{\partial\gamma}.$$

With these spaces and forms, the weak form of Eq. 3 may be written as follows:

$$\begin{aligned} & \mathbf{u} \in \mathbf{W}, p \in M \\ (\mathcal{P}) \quad & a(\mathbf{u}, \mathbf{v}) - b(\mathbf{v}, p) = L_d(\mathbf{v}) \quad \forall \mathbf{v} \in \mathbf{W} \\ & b(\mathbf{u}, r) = L_q(r) \quad \forall r \in M. \end{aligned} \quad (4)$$

That Eq. 4 has a unique solution is shown in [17].

For convenience of notation, we also define the spaces H , \mathbf{H} , and \mathbf{M} as follows:

$$H = H^1(\Omega_1) \times H^1(\Omega_2) \times H^1(\gamma) \subset M$$

$$\mathbf{H} = (H^1(\Omega_1))^n \times (H^1(\Omega_2))^n \times (H^1(\gamma))^{n-1} \subset \mathbf{W}$$

$$\mathbf{M} = (L^2(\Omega_1))^n \times (L^2(\Omega_2))^n \times (L^2(\gamma))^{n-1} \supset \mathbf{W}$$

with their product norms. We clearly have that the inclusions $H \hookrightarrow M$ and $\mathbf{H} \hookrightarrow \mathbf{W} \hookrightarrow \mathbf{M}$ are continuous and dense (since $\|\mathbf{v}_i \cdot \mathbf{n}\|_{0,\gamma} \leq C \|\mathbf{v}_i\|_{1,\Omega_i}$; $i = 1, 2$ for $\mathbf{v} \in \mathbf{H}$). Also to shorten notation, we shall write for $\mathbf{v} \in \mathbf{W}$,

$$\text{div } \mathbf{v} = (\text{div } \mathbf{v}_1, \text{div } \mathbf{v}_2, \text{div}_\tau \mathbf{v}_\gamma) \quad \text{and}$$

$$\text{Div } \mathbf{v} = (\text{div } \mathbf{v}_1, \text{div } \mathbf{v}_2, \text{div}_\tau \mathbf{v}_\gamma - [\mathbf{v} \cdot \mathbf{n}]).$$

4 Discretization and error estimates

Let $\mathcal{T}_{h,i}$ be a finite element partition of Ω_i , $i = 1, 2$, made up of n -dimensional simplicial and/or rectangular elements, and $\mathcal{T}_{h,\gamma}$ a finite element partition of γ made up of $(n-1)$ -dimensional simplicial and/or rectangular elements with no matching requirements between any of these partitions. The associated approximation spaces are for the scalar variable

$$M_h = M_{h,1} \times M_{h,2} \times M_{h,\gamma},$$

where $M_{h,i}$, $i = 1, 2$, respectively; $M_{h,\gamma}$, is the space of piecewise constant functions associated with $\mathcal{T}_{h,i}$, $i = 1, 2$, respectively $\mathcal{T}_{h,\gamma}$; and for the vector variable

$$\mathbf{W}_h = \mathbf{W}_{h,1} \times \mathbf{W}_{h,2} \times \mathbf{W}_{h,\gamma},$$

where $\mathbf{W}_{h,i}$, $i = 1, 2$, respectively $\mathbf{W}_{h,\gamma}$, is the lowest-order Raviart–Thomas(–Nedelec) space associated with $\mathcal{T}_{h,i}$, $i = 1, 2$, respectively $\mathcal{T}_{h,\gamma}$. Recall that $\mathbf{W}_{h,i}$, $i = 1, 2$, respectively $\mathbf{W}_{h,\gamma}$, is the set of functions in $H(\text{div}, \Omega_i)$, $i = 1, 2$ respectively $H(\text{div}_\tau, \gamma)$, whose restrictions to n -simplicial elements are of the form $(a_1 + b x_1, \dots, a_n + b x_n)^t$, and whose restrictions to n -rectangular elements are of the form $(a_1 + b_1 x_1, \dots, a_n + b_n x_n)^t$.

Thus $\mathbf{W}_h \subset \mathbf{W}$ and $M_h \subset M$, and the discrete mixed problem may be written as follows:

$$(\mathcal{P}_h) \quad \begin{aligned} &\mathbf{u}_h \in \mathbf{W}_h, \quad p_h \in M_h \\ &a(\mathbf{u}_h, \mathbf{v}_h) - b(\mathbf{v}_h, p_h) = L_d(\mathbf{v}_h) \quad \forall \mathbf{v}_h \in \mathbf{W}_h \\ &b(\mathbf{u}_h, r_h) = L_q(r_h) \quad \forall r_h \in M_h. \end{aligned} \quad (5)$$

4.1 Interpolation estimates

The following projection operators will be needed for the analysis: for $i=1,2$, let $\Pi_{h,i}$ be the Raviart–Thomas projection onto $\mathbf{W}_{h,i}$, which satisfies that for any $\mathbf{v}_i \in (H^1(\Omega_i))^n \cap \mathbf{W}_i$,

$$\begin{aligned} &(\text{div}(\Pi_{h,i} \mathbf{v}_i - \mathbf{v}_i), r_{h,i})_{\Omega_i} = 0 \\ &\quad \forall r_{h,i} \in M_{h,i}, \\ &\langle (\mathbf{v}_i - \Pi_{h,i} \mathbf{v}_i) \cdot \mathbf{n}_i, \mathbf{w}_{h,i} \cdot \mathbf{n}_i \rangle_{\partial \Omega_i} = 0 \\ &\quad \forall \mathbf{w}_{h,i} \in \mathbf{W}_{h,i}, \end{aligned} \quad (6)$$

and let $\pi_{h,i}$ be the L^2 projection onto $M_{h,i}$ satisfying for any $q_i \in L^2(\Omega_i)$

$$(\pi_{h,i} q_i - q_i, r_{h,i})_{\Omega_i} = 0 \quad \forall r_{h,i} \in M_{h,i}. \quad (7)$$

Similarly, let $\Pi_{h,\gamma}$ be the Raviart–Thomas projection onto $\mathbf{W}_{h,\gamma}$, which satisfies that for any $\mathbf{v}_\gamma \in (H^1(\gamma))^{n-1} \cap \mathbf{W}_\gamma$,

$$\begin{aligned} &(\text{div}_\tau(\Pi_{h,\gamma} \mathbf{v}_\gamma - \mathbf{v}_\gamma), r_{h,\gamma})_\gamma = 0 \\ &\quad \forall r_{h,\gamma} \in M_{h,\gamma}, \\ &\langle (\mathbf{v}_\gamma - \Pi_{h,\gamma} \mathbf{v}_\gamma) \cdot \mathbf{n}_\gamma, \mathbf{w}_{h,\gamma} \cdot \mathbf{n}_\gamma \rangle_{\partial \gamma} = 0 \\ &\quad \forall \mathbf{w}_{h,\gamma} \in \mathbf{W}_{h,\gamma}, \end{aligned} \quad (8)$$

and let $\pi_{h,\gamma}$ be the L^2 projection onto $M_{h,\gamma}$ satisfying for any $q_\gamma \in L^2(\gamma)$

$$(\pi_{h,\gamma} q_\gamma - q_\gamma, r_{h,\gamma})_\gamma = 0 \quad \forall r_{h,\gamma} \in M_{h,\gamma}. \quad (9)$$

These projection operators are known to have the following approximation properties: for $q = (q_1, q_2, q_\gamma) \in M$ and $\mathbf{v} = (\mathbf{v}_1, \mathbf{v}_2, \mathbf{v}_\gamma) \in \mathbf{H}$ and for $\rho \in \mathbb{R}$; $0 \leq \rho \leq 1$, and for $i = 1, 2$,

$$\|q_i - \pi_{h,i} q_i\|_{0,\Omega_i} \leq C h^\rho \|q_i\|_{\rho,\Omega_i}, \quad (10)$$

$$\|q_\gamma - \pi_{h,\gamma} q_\gamma\|_{0,\gamma} \leq C h^\rho \|q_\gamma\|_{\rho,\gamma}, \quad (11)$$

$$\|\mathbf{v}_i - \Pi_{h,i} \mathbf{v}_i\|_{0,\Omega_i} \leq C h \|\mathbf{v}_i\|_{1,\Omega_i}, \quad (12)$$

$$\|\mathbf{v}_\gamma - \Pi_{h,\gamma} \mathbf{v}_\gamma\|_{0,\gamma} \leq C h \|\mathbf{v}_\gamma\|_{1,\gamma}, \quad (13)$$

$$\|\text{div}(\mathbf{v}_i - \Pi_{h,i} \mathbf{v}_i)\|_{0,\Omega_i} \leq C h^\rho \|\text{div} \mathbf{v}_i\|_{\rho,\Omega_i}. \quad (14)$$

$$\|\text{div}_\tau(\mathbf{v}_\gamma - \Pi_{h,\gamma} \mathbf{v}_\gamma)\|_{0,\gamma} \leq C h^\rho \|\text{div}_\tau \mathbf{v}_\gamma\|_{\rho,\gamma}, \quad (15)$$

$$\|(\mathbf{v}_i - \Pi_{h,i} \mathbf{v}_i) \cdot \mathbf{n}_i\|_{0,\gamma} \leq C h^\rho \|\mathbf{v}_i \cdot \mathbf{n}_i\|_{\rho,\gamma}, \quad (16)$$

whenever \mathbf{v} and q are regular enough for the righthand side to be defined. (See [20, Theorem 6.3] or [8] for Eqs. 12 and 13. The other estimates, Eqs. 10, 11, 14, 15, and 16, are standard estimates for L^2 -projections.) Then defining $\pi_h : M \rightarrow M_h$, respectively $\Pi_h : \mathbf{H} \rightarrow \mathbf{W}_h$ to be the product of $\pi_{h,1}$ with $\pi_{h,2}$ and $\pi_{h,\gamma}$, respectively $\Pi_{h,1}$ with $\Pi_{h,2}$ and $\Pi_{h,\gamma}$, we clearly have the following estimates: for $q \in H$ and $\mathbf{v} \in \mathbf{H}$

$$\|q - \pi_h q\|_M \leq C h \|q\|_H, \quad (17)$$

$$\|\mathbf{v} - \Pi_h \mathbf{v}\|_{\mathbf{W}} \leq C h \|\mathbf{v}\|_{\mathbf{H}}, \quad (18)$$

$$\|\text{div}(\mathbf{v} - \Pi_h \mathbf{v})\|_M \leq C h \|\text{div} \mathbf{v}\|_H, \quad (19)$$

so that

$$\|\mathbf{v} - \Pi_h \mathbf{v}\|_{\mathbf{W}} \leq C h \left\{ \|\mathbf{v}\|_{\mathbf{H}} + \|\text{div} \mathbf{v}\|_H + \sum_{i=1}^2 \|\mathbf{v}_i \cdot \mathbf{n}_i\|_{1,\gamma} \right\}, \quad (20)$$

whenever $\text{div} \mathbf{v} \in H$ and $\mathbf{v}_i \cdot \mathbf{n}_i \in H^1(\gamma)$, $i = 1, 2$. It is also clear that both of these maps are continuous:

$$\begin{aligned} \|\pi_h q\|_M &\leq \|q\|_M, \quad \forall q \in M \\ \|\Pi_h \mathbf{v}\|_{\mathbf{W}} &\leq C \|\mathbf{v}\|_{\mathbf{H}}, \quad \forall \mathbf{v} \in \mathbf{H}, \end{aligned} \quad (21)$$

where the first inequality is well known for L^2 -projections, and the second follows from Eqs. 12 and 13 and from Eqs. 14, 15, and 16 with $\rho = 0$. Recalling the definition of $\text{Div} : \mathbf{W} \rightarrow M$ and defining $\text{Div}_h : \mathbf{W}_h \rightarrow M_h$ by

$$\begin{aligned} \text{Div}(\mathbf{v}) &= (\text{div} \mathbf{v}_1, \text{div} \mathbf{v}_2, \text{div}_\tau \mathbf{v}_\gamma - [\mathbf{v} \cdot \mathbf{n}]) \\ \text{Div}_h(\mathbf{v}_h) &= (\text{div} \mathbf{v}_{h,1}, \text{div} \mathbf{v}_{h,2}, \text{div}_\tau \mathbf{v}_{h,\gamma} - \pi_{h,\gamma}[\mathbf{v}_h \cdot \mathbf{n}]), \end{aligned}$$

except for the case of matching grids, we note that we do not have commutativity of the diagram

$$\begin{array}{ccc} \mathbf{H} & \xrightarrow{\text{Div}} & M \\ \downarrow \Pi_h & & \downarrow \pi_h \\ \mathbf{W}_h & \xrightarrow{\text{Div}_h} & M_h, \end{array}$$

i.e., in general

$$\text{Div}_h \Pi_h \mathbf{v} \neq \pi_h \text{Div} \mathbf{v},$$

for nonmatching grids, even though we do have

$$\begin{aligned} \text{div} \Pi_{h,i} \mathbf{v}_i &= \pi_{h,i} \text{div} \mathbf{v}_i, \quad \forall \mathbf{v}_i \in (H^1(\Omega_i))^n, \\ &\quad i = 1, 2, \\ \text{div}_\tau \Pi_{h,\gamma} \mathbf{v}_\gamma &= \pi_{h,\gamma} \text{div}_\tau \mathbf{v}_\gamma, \quad \forall \mathbf{v}_\gamma \in (H^1(\gamma))^{n-1}. \end{aligned}$$

This is due to the fact that, in general, for nonmatching grids

$$\pi_{h,\gamma}(\mathbf{v}_i \cdot \mathbf{n}) \neq \pi_{h,\gamma}(\Pi_{h,i} \mathbf{v}_i \cdot \mathbf{n}) \quad i = 1, 2. \quad (22)$$

This can be seen in particular when the space $M_{h,\gamma}$ is much richer than the space of normal traces on γ of elements of $\mathbf{W}_{h,i}$.

4.2 Approximation estimates

The proof of the existence and uniqueness of the solution of the discrete problem (5) as well as the error estimates will follow from Lemmas 1 and 2 given next. All of the demonstrations follow closely those in [17].

Lemma 1 *With the hypotheses made concerning the permeabilities and the fracture width and with the assumption that $\xi > \frac{1}{2}$ the bilinear form $a(\cdot, \cdot)$ is elliptic on the space $\tilde{\mathbf{W}}_h$,*

$$\tilde{\mathbf{W}}_h = \{\mathbf{v}_h \in \mathbf{W}_h : b(\mathbf{v}_h, r_h) = 0, \quad \forall r_h \in M_h\},$$

with a constant independent of h , i.e., there exists a constant $C_a > 0$ such that

$$a(\mathbf{v}_h, \mathbf{v}_h) \geq C_a \|\mathbf{v}_h\|_{\mathbf{W}}^2, \quad \forall \mathbf{v}_h \in \tilde{\mathbf{W}}_h.$$

Proof Suppose $\mathbf{v}_h \in \tilde{\mathbf{W}}_h$, and consider the test function $r_h \in M_h$ in Eq. 5 defined by $r_h = (\text{div} \mathbf{v}_{h,1}, \text{div} \mathbf{v}_{h,2}, \text{div}_\tau \mathbf{v}_{h,\gamma} - \pi_{h,\gamma}[\mathbf{v}_h \cdot \mathbf{n}])$. Then

$$\begin{aligned} 0 = b(\mathbf{v}_h, r_h) &= \sum_{i=1}^2 \|\text{div} \mathbf{v}_{h,i}\|_{0,\Omega_i}^2 \\ &\quad + \|\text{div}_\tau \mathbf{v}_{h,\gamma} - \pi_{h,\gamma}[\mathbf{v}_h \cdot \mathbf{n}]\|_{0,\gamma}^2, \end{aligned}$$

and we have

$$\text{div} \mathbf{v}_{h,i} = 0, \quad i = 1, 2$$

$$\text{div}_\tau \mathbf{v}_{h,\gamma} = \pi_{h,\gamma}[\mathbf{v}_h \cdot \mathbf{n}].$$

Thus, using Eq. 21 it follows that

$$\begin{aligned} \|\mathbf{v}_h\|_{\mathbf{W}}^2 &\leq \sum_{i=1}^2 \|\mathbf{v}_{h,i}\|_{0,\Omega_i}^2 + \|\mathbf{v}_{h,\gamma}\|_{0,\gamma}^2 \\ &\quad + 3 \sum_{i=1}^2 \|\mathbf{v}_{h,i} \cdot \mathbf{n}\|_{0,\gamma}^2. \end{aligned}$$

Also a can be written as follows:

$$\begin{aligned} a(\mathbf{v}_h, \mathbf{v}_h) &= \sum_{i=1}^2 (\mathbf{K}_i^{-1} \mathbf{v}_{h,i}, \mathbf{v}_{h,i})_{\Omega_i} \\ &\quad + (\mathbf{K}_\gamma^{-1} \mathbf{v}_{h,\gamma}, \mathbf{v}_{h,\gamma})_\gamma \\ &\quad + \xi \sum_{i=1}^2 \left(\frac{\mathbf{v}_{h,i} \cdot \mathbf{n}}{\kappa_\gamma^{1/2}}, \frac{\mathbf{v}_{h,i} \cdot \mathbf{n}}{\kappa_\gamma^{1/2}} \right)_\gamma \\ &\quad + 2 \bar{\xi} \left(\frac{\mathbf{v}_{h,1} \cdot \mathbf{n}}{\kappa_\gamma^{1/2}}, \frac{\mathbf{v}_{h,2} \cdot \mathbf{n}}{\kappa_\gamma^{1/2}} \right)_\gamma. \end{aligned} \quad (23)$$

So, for $\mathbf{v}_h \in \tilde{\mathbf{W}}_h$,

$$\begin{aligned} a(\mathbf{v}_h, \mathbf{v}_h) &\geq C \left(\sum_{i=1}^2 \|\mathbf{v}_{h,i}\|_{0,\Omega_i}^2 + \|\mathbf{v}_{h,\gamma}\|_{0,\gamma}^2 \right) \\ &\quad + \min\{1, \xi - \bar{\xi}\} \sum_{i=1}^2 \left\| \frac{\mathbf{v}_{h,i} \cdot \mathbf{n}}{\kappa_\gamma^{1/2}} \right\|_{0,\gamma}^2 \\ &\geq C(\mathbf{K}_1, \mathbf{K}_2, \mathbf{K}_\gamma, \kappa_\gamma, \xi) \|\mathbf{v}_h\|_{\mathbf{W}}^2, \end{aligned}$$

where the constant $C_a = C(\mathbf{K}_1, \mathbf{K}_2, \mathbf{K}_\gamma, \kappa_\gamma, \xi) > 0$ depends on the permeability tensor \mathbf{K} , the width function d on the fracture and the quadrature parameter $\xi > \frac{1}{2}$ but not on the mesh parameter h . \square

Lemma 2 *The bilinear form $b : \mathbf{W}_h \times M_h \rightarrow \mathbb{R}$ satisfies the inf-sup condition with a constant independent of h , i.e., there exists a constant $C_b > 0$ such that*

$$\forall r_h \in M_h, \quad \sup_{\mathbf{v}_h \in \mathbf{W}_h} \frac{b(\mathbf{v}_h, r_h)}{\|\mathbf{v}_h\|_{\mathbf{W}}} \geq C_b \|r_h\|_M.$$

Proof Given $r_h \in M_h$, using auxillary problems, we construct an element $\mathbf{v}_h \in \mathbf{W}_h$ such that $b(\mathbf{v}_h, r_h) = \|r_h\|_M^2$ and $\|\mathbf{v}_h\|_{\mathbf{W}} \leq C \|r_h\|_M$, where C depends on

the constants of elliptic regularity for the auxillary problems.

For $r_h = (r_{h,1}, r_{h,2}, r_{h,\gamma}) \in M_h$, let $\zeta \in H^2(\Omega)$ be the solution of

$$\begin{aligned} -\Delta \zeta &= \tilde{r}_h && \text{in } \Omega, \\ \zeta &= 0 && \text{on } \partial\Omega, \end{aligned} \quad (24)$$

where $\tilde{r}_h \in L^2(\Omega)$ is given by $\tilde{r}_{h,i} = r_{h,i}$, $i = 1, 2$. Pose $\mathbf{v}_i = -\nabla \zeta|_{\Omega_i}$, $i = 1, 2$, and let $\mathbf{v}_{h,i} = \Pi_{h,i} \mathbf{v}_i$. Then

$$\begin{aligned} \operatorname{div} \mathbf{v}_{h,i} &= \operatorname{div} \Pi_{h,i} \mathbf{v}_i = \pi_{h,i} \operatorname{div} \mathbf{v}_i \\ &= \pi_{h,i} r_{h,i} = r_{h,i}. \end{aligned}$$

Next, let $\zeta_\gamma \in H^2(\gamma)$ be the solution of

$$\begin{aligned} -\Delta_\tau \zeta_\gamma &= r_{h,\gamma} + \pi_{h,\gamma} [\mathbf{v}_h \cdot \mathbf{n}] && \text{in } \gamma, \\ \zeta_\gamma &= 0 && \text{on } \partial\gamma, \end{aligned} \quad (25)$$

where we note that even though $[\mathbf{v} \cdot \mathbf{n}] = 0$, in general with nonmatching grids, $[\mathbf{v}_h \cdot \mathbf{n}] \neq 0$ and $\pi_{h,\gamma} [\mathbf{v}_h \cdot \mathbf{n}] \neq 0$, cf. (Eq. 22). Pose $\mathbf{v}_\gamma = -\nabla_\tau \zeta_\gamma$, and let $\mathbf{v}_{h,\gamma} = \Pi_{h,\gamma} \mathbf{v}_\gamma$. Then, we have the following:

$$\begin{aligned} \operatorname{div}_\tau \mathbf{v}_{h,\gamma} &= \operatorname{div}_\tau \Pi_{h,\gamma} \mathbf{v}_\gamma = \pi_{h,\gamma} \operatorname{div}_\tau \mathbf{v}_\gamma \\ &= r_{h,\gamma} + \pi_{h,\gamma} [\mathbf{v}_h \cdot \mathbf{n}]. \end{aligned}$$

Thus, $\mathbf{v}_h = (\mathbf{v}_{h,1}, \mathbf{v}_{h,2}, \mathbf{v}_{h,\gamma}) \in \mathbf{W}_h$ and

$$\begin{aligned} b(\mathbf{v}_h, r_h) &= \sum_{i=1}^2 (r_{h,i}, r_{h,i})_{\Omega_i} \\ &\quad + (r_{h,\gamma} + \pi_{h,\gamma} [\mathbf{v}_h \cdot \mathbf{n}], r_{h,\gamma})_\gamma \\ &\quad - (\pi_{h,\gamma} [\mathbf{v}_h \cdot \mathbf{n}], r_{h,\gamma})_\gamma, \\ &= \|r_h\|_M^2. \end{aligned}$$

To bound $\|\mathbf{v}_h\|_{\mathbf{W}}^2$ in terms of $\|r_h\|_M$, we recall that

$$\begin{aligned} \|\mathbf{v}_h\|_{\mathbf{W}}^2 &= \sum_{i=1}^2 (\|\mathbf{v}_{h,i}\|_{0,\Omega_i}^2 + \|\operatorname{div} \mathbf{v}_{h,i}\|_{0,\Omega_i}^2) \\ &\quad + \|\mathbf{v}_{h,\gamma}\|_{0,\gamma}^2 + \|\operatorname{div}_\tau \mathbf{v}_{h,\gamma}\|_{0,\gamma}^2 \\ &\quad + \sum_{i=1}^2 \|\mathbf{v}_{h,i} \cdot \mathbf{n}\|_{0,\gamma}^2 \end{aligned}$$

and treat the terms separately. For the first term, we have

$$\begin{aligned} \sum_{i=1}^2 \|\mathbf{v}_{h,i}\|_{0,\Omega_i}^2 &= \sum_{i=1}^2 \|\Pi_{h,i} \mathbf{v}_i\|_{0,\Omega_i}^2 \\ &\leq C \sum_{i=1}^2 \|\mathbf{v}_i\|_{1,\Omega_i}^2 \\ &= C \sum_{i=1}^2 \|\nabla \zeta\|_{1,\Omega_i}^2 \\ &= C \|\nabla \zeta\|_{1,\Omega}^2 \\ &\leq C \|\zeta\|_{2,\Omega}^2 \\ &\leq C(\Omega) \|\tilde{r}_h\|_{0,\Omega}^2, \end{aligned}$$

and for the second term, we have immediately

$$\sum_{i=1}^2 \|\operatorname{div} \mathbf{v}_{h,i}\|_{0,\Omega_i}^2 = \sum_{i=1}^2 \|r_{h,i}\|_{0,\Omega_i}^2.$$

The third term is estimated quite similarly to the first term:

$$\begin{aligned} \|\mathbf{v}_{h,\gamma}\|_{0,\gamma}^2 &= \|\Pi_{h,\gamma} \mathbf{v}_\gamma\|_{0,\gamma}^2 \leq C \|\mathbf{v}_\gamma\|_{1,\gamma}^2 \\ &= C \|\nabla_\tau \zeta_\gamma\|_{1,\gamma}^2 \leq C \|\zeta_\gamma\|_{2,\gamma}^2 \\ &\leq C(\gamma) \|r_{h,\gamma} + \pi_{h,\gamma} [\mathbf{v}_h \cdot \mathbf{n}]\|_{0,\gamma}^2 \\ &\leq C (\|r_{h,\gamma}\|_{0,\gamma}^2 + \|[\mathbf{v}_h \cdot \mathbf{n}]\|_{0,\gamma}^2) \\ &\leq C \left(\|r_{h,\gamma}\|_{0,\gamma}^2 + \sum_{i=1}^2 \|(\mathbf{v}_i - \mathbf{v}_{h,i}) \cdot \mathbf{n}\|_{0,\gamma}^2 \right) \\ &\leq C \left(\|r_{h,\gamma}\|_{0,\gamma}^2 + \sum_{i=1}^2 \|\mathbf{v}_i\|_{1,\Omega_i}^2 \right) \\ &\leq C \left(\|r_{h,\gamma}\|_{0,\gamma}^2 + \sum_{i=1}^2 \|r_{h,i}\|_{0,\Omega_i}^2 \right), \end{aligned}$$

where we have used the fact $[\mathbf{v} \cdot \mathbf{n}] = 0$, the estimate (Eq. 16), and the continuity of the trace operator. For the fourth term, we have

$$\begin{aligned} \|\operatorname{div}_\tau \mathbf{v}_{h,\gamma}\|_{0,\gamma}^2 &= \|r_{h,\gamma} + \pi_{h,\gamma} [\mathbf{v}_h \cdot \mathbf{n}]\|_{0,\gamma}^2 \\ &\leq C \left(\|r_{h,\gamma}\|_{0,\gamma}^2 + \sum_{i=1}^2 \|r_{h,i}\|_{0,\Omega_i}^2 \right). \end{aligned}$$

Finally, for the last term, we obtain

$$\begin{aligned} \sum_{i=1}^2 \|\mathbf{v}_{h,i} \cdot \mathbf{n}\|_{0,\gamma}^2 &= \sum_{i=1}^2 \|\Pi_{h,i} \mathbf{v}_i \cdot \mathbf{n}\|_{0,\gamma}^2 \\ &\leq \sum_{i=1}^2 \|\mathbf{v}_i \cdot \mathbf{n}\|_{0,\gamma}^2 \\ &\leq C \sum_{i=1}^2 \|\mathbf{v}_i\|_{1,\Omega_i}^2 \\ &\leq C \sum_{i=1}^2 \|r_{h,i}\|_{0,\Omega_i}^2. \end{aligned}$$

Thus, the constant $C = C(\Omega_1, \Omega_2, \gamma)$ is independent of h . \square

Applying Brezzi's theorem [20, Theorem 10.4] and using Lemmas 1 and 2 we obtain the following theorem:

Theorem 1 *If $(\mathbf{u}, p) \in \mathbf{W} \times M$ is the solution of problem (\mathcal{P}) and $(\mathbf{u}_h, p_h) \in \mathbf{W}_h \times M_h$ is the solution of problem (\mathcal{P}_h) , then*

$$\begin{aligned} \|p - p_h\|_M + \|\mathbf{u} - \mathbf{u}_h\|_{\mathbf{W}} \\ \leq C \left(\inf_{q_h \in M_h} \|p - q_h\|_M + \inf_{\mathbf{v}_h \in \mathbf{W}_h} \|\mathbf{u} - \mathbf{v}_h\|_{\mathbf{W}} \right). \end{aligned}$$

Combining Theorem 1 with the interpolation estimates Eqs. 17 and 20, we obtain

Theorem 2 *If $(\mathbf{u}, p) \in \mathbf{W} \times M$ is the solution of problem (\mathcal{P}) and $(\mathbf{u}_h, p_h) \in \mathbf{W}_h \times M_h$ is the solution of problem (\mathcal{P}_h) , and \mathbf{u} and p are sufficiently regular, then*

$$\begin{aligned} \|p - p_h\|_M + \|\mathbf{u} - \mathbf{u}_h\|_{\mathbf{W}} \\ \leq Ch \left(\|p\|_H + \|\mathbf{u}\|_{\mathbf{H}} + \|\operatorname{div} \mathbf{u}\|_H + \sum_{i=1}^2 \|\mathbf{v}_i \cdot \mathbf{n}\|_{1,\gamma} \right). \end{aligned} \quad (26)$$

Remark 1 Theorem 2 states that the discrete fracture system (\mathcal{P}) with nonconforming meshes yields optimal order convergence ($\mathcal{O}(h)$) for sufficiently smooth solutions. No hypotheses are made concerning the mesh sizes on the interface. The spaces (the lowest-order Raviart–Thomas spaces for the velocity, and piecewise constants for the pressure) are the standard ones: in particular, in contrast to what is generally done for the mortar method [6], we assumed that the polynomials

of the interface-pressure finite-element space are of the same order as those of the space of the normal traces on the interface of the subdomain velocities.

5 Numerical results

In this section, we present some numerical results that confirm the convergence estimate provided in Theorem 2. Several cases are shown to illustrate the very different flow regimes the fracture model can handle: in Section 5.1, the fracture is highly permeable, whereas in Section 5.2, it represents a barrier with a very low permeability. In Section 5.3, a fracture with an anisotropic permeability is considered, and in Section 5.4, a fracture with the same permeability as the surrounding medium is considered in order to carry out a comparison with a mortar method.

As stated earlier, we have assumed that the discretization mesh \mathcal{T}_h respects the fracture, but that the meshes on Ω_1 , Ω_2 and γ may be chosen independently. We will say that the mesh $\mathcal{T}_h = (\mathcal{T}_{h1}, \mathcal{T}_{h2}, \mathcal{T}_{h\gamma})$ is made up of three meshes with \mathcal{T}_{hi} being a mesh on Ω_i , $i = 1, 2$, and $\mathcal{T}_{h\gamma}$ being a mesh of γ . In all of the experiments reported here, for $i = 1, 2$, \mathcal{T}_{hi} has been taken to be a uniform mesh made up of squares of edge-length h_i and $\mathcal{T}_{h\gamma}$ to be a uniform mesh made up of intervals of length h_γ . The mesh parameter h for \mathcal{T}_h is

$$h = \max\{h_1, h_2, h_\gamma\}.$$

In this case, to say that the grid is conforming simply means that $h_1 = h_2 = h_\gamma$.

In some interface integrals in Eq. 5, the functions to be integrated live in different discretization spaces: $(\mathbf{u}_{i+1} \cdot \mathbf{n}, \mathbf{v}_i \cdot \mathbf{n})_\gamma$ (mesh 1 and mesh 2) or $(\mathbf{u}_i \cdot \mathbf{n}, r_\gamma)_\gamma$ (mesh i and the interface mesh). With the lowest order spaces M_h and \mathbf{W}_h , the computation of these integrals reduces simply to computing the measures of the intersections of elements from the two different meshes. In the present two dimensional case, it is quite easy to compute numerically the measure of the intersection of two segments. In three dimensions, the problem is more involved; for tetrahedral meshes, one needs to compute efficiently the measure of the intersection of all pairs of intersecting triangles from the two different meshes (see for instance [1]).

In the experiments that follow, we denote by (p_h, \mathbf{u}_h) the solution of (\mathcal{P}_h) obtained with a *nonconforming* mesh \mathcal{T}_h . In the convergence computations, the parameters determining \mathcal{T}_h were taken as follows: $h_1 = 1/n$, $h_2 = 1/(n+8)$ and $h_\gamma = 1/(10n)$ for the case of finer discretization in the fracture or $h_\gamma = 5/n$ for the

Table 1 Number of cells (segments) on the interface from each of the two subdomain discretizations and from the fracture discretization (coarse case and fine case) for the various mesh refinements

	\mathcal{T}_1	\mathcal{T}_2	\mathcal{T}_3	\mathcal{T}_4	\mathcal{T}_5	\mathcal{T}_6	\mathcal{T}_7	\mathcal{T}_8
$N_{y,1}$	20	40	80	100	160	200	400	600
$N_{y,2}$	28	48	88	108	168	208	408	608
$N_{y,f}^{\text{coarse}}$	4	8	16	20	32	40	80	120
$N_{y,f}^{\text{fine}}$	200	400	800	1,000	1,600	2,000	4,000	6,000

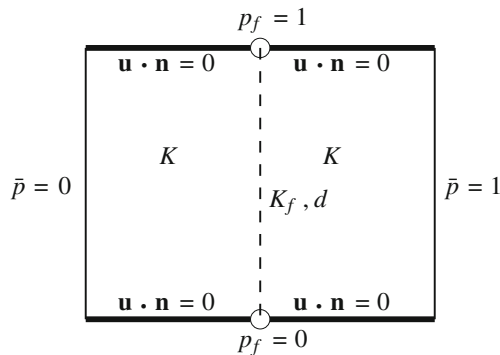


Fig. 1 Test case 1 with a large permeability in the fracture. Homogeneous Neumann boundary conditions are depicted with fat lines. The fracture is depicted with a dashed line

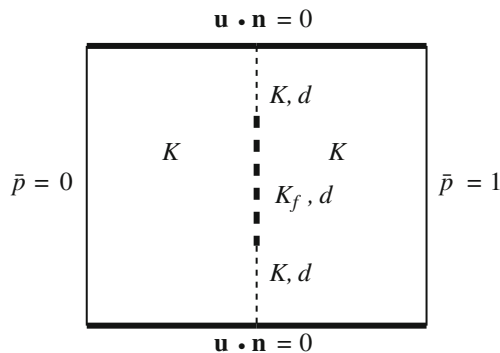


Fig. 2 Test case 2 with a geological barrier. The impervious part of the fracture is limited to the central zone

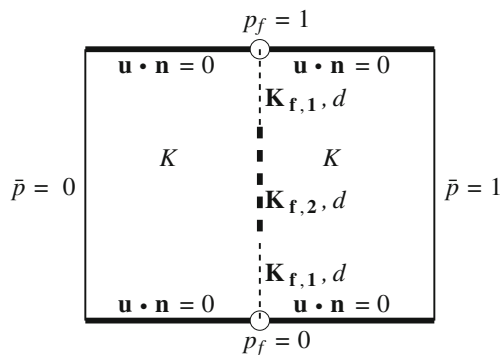


Fig. 3 Test case 3 with an anisotropic, heterogeneous permeability

case of a coarser discretization in the fracture, for some $n \in [20, 600]$ (see Table 1). We point out that in order to depict the solutions, both pressure and velocity, we have used a rather coarse mesh so that the mesh as well as the arrows representing the velocity may be clearly seen.

In all of the experiments, the numerical parameter ξ in the fifth equation of model (3) is taken to be $\xi = 2/3$. We experimented with other values of ξ , in particular $\xi = 1$, but the results were identical for the experiments of Sections 5.1, 5.2, and 5.4 (not shown here for the sake of brevity). For the results of Section 5.3, some small differences appear that do not have an effect on the conclusions.

In order to compute relative L^2 errors for the pressure and Darcy velocity, we calculate a *reference solution* $(\mathbf{u}_\eta^*, p_\eta^*)$ which is the solution of (\mathcal{P}_h) obtained with a *conforming mesh* \mathcal{T}_η^* , (i.e. $\eta_1 = \eta_2 = \eta_\gamma = \eta$) with $\eta <$

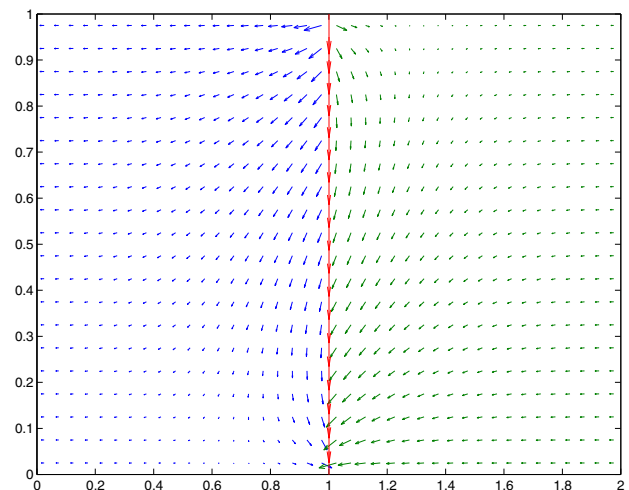
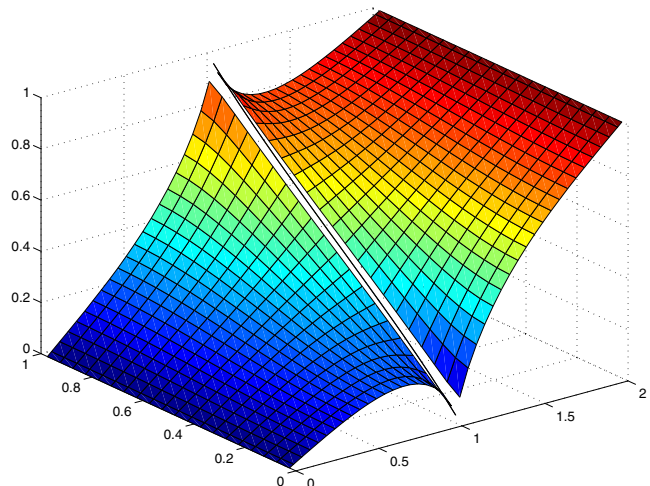


Fig. 4 Test case 1. Pressure (top) and Darcy velocity (bottom) with conforming meshes ($h_1 = h_2 = h_\gamma = 1/20$). $K_f = 2000$, $d = 0.001$. (The grids are quite coarse for visualization purposes)

h whenever h is the mesh parameter in the experiment under consideration. (Here, $\eta = 1/1200$.)

The L^2 errors are approximated as follows: the “intersection mesh” (coarsest common refinement) $\mathcal{T}_\eta^* \cap \mathcal{T}_h$ is computed (in each subdomain and in γ). Then, the reference $(\mathbf{u}_\eta^*, p_\eta^*)$ and nonconforming (\mathbf{u}_h, p_h) solutions are interpolated on this intersection mesh. The difference is computed, squared, and numerically integrated to obtain $\|p_h - p_\eta^*\|_M^2$ and $\|\mathbf{u}_h - \mathbf{u}_\eta^*\|_M^2$. Thus, these take into account errors in the fracture and errors in the subdomains. With sufficient regularity and with h not of the same order as η , these norms should behave as $\mathcal{O}(h)$ according to Theorem 2.

In all test cases, the domain is a 2 by 1 rectangle with the fracture interface γ being the central vertical bisector, so that Ω_1 and Ω_2 are the remaining lefthand and righthand squares when γ is removed from the domain.

In all test cases, the permeability in the subdomains is scalar with $K_1 = K_2 = 1$, the tops and bottoms of the two subdomains are impermeable, and there is a pressure drop from the righthand side of the domain to the lefthand side of the domain. The width d of the physical fracture is $d = 0.001$. The permeability K_f in the fracture is scalar in the first, second, and fourth test cases and is anisotropic in the third.

In the first test case, the fracture is highly permeable and there is a pressure drop from the top to the bottom of the fracture so that the fluid flows along the fracture as well as from right to left (see Fig. 1). In the second test case, the central part of the fracture is a barrier with very low permeability so that the fluid flows from right to left but must flow around the fracture (see Fig. 2). In the third test case, the fracture is anisotropic and is separated into three zones (see Fig. 3). In the central

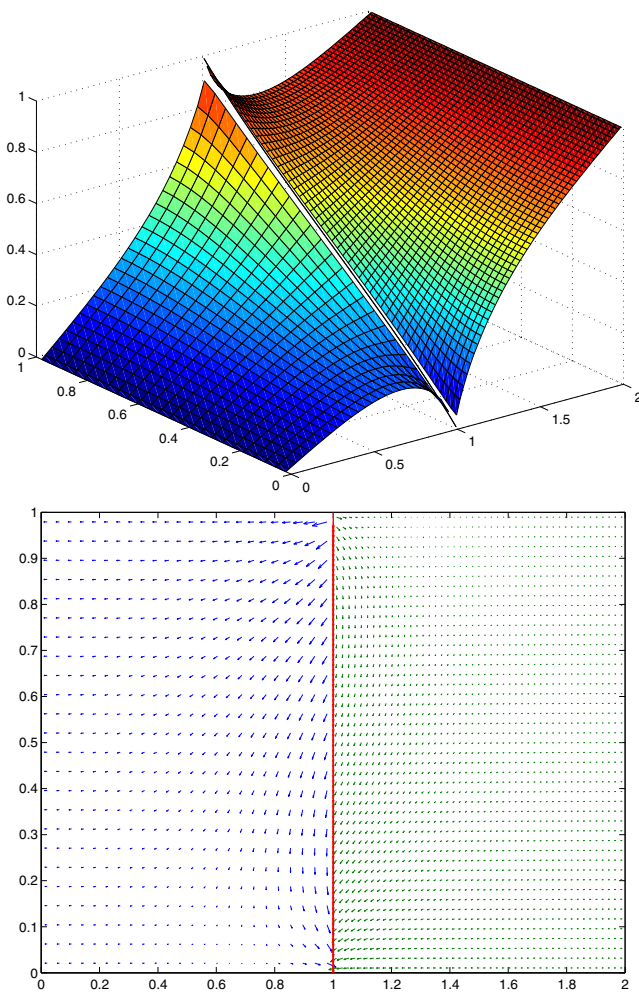


Fig. 5 Test case 1. Pressure (top) and Darcy velocity (bottom) with nonconforming meshes: $h_1 = 1/24$, $h_\gamma = 1/91$, $h_2 = 1/47$ (the fracture mesh is finer than the other meshes). $K_f = 2000$, $d = 0.001$

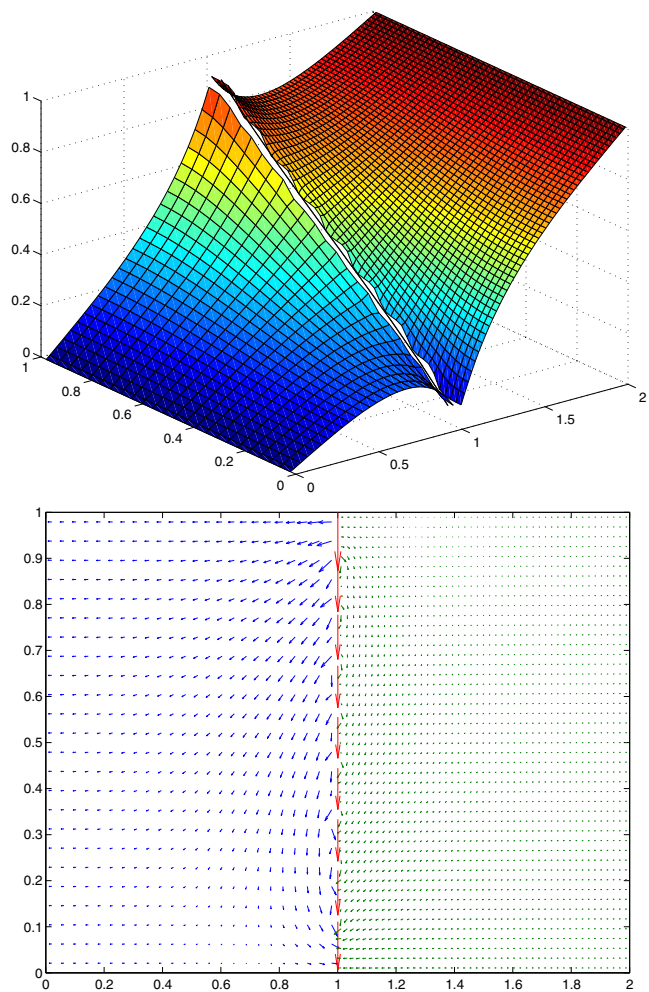


Fig. 6 Test case 1. Pressure (top) and Darcy velocity (bottom) with nonconforming meshes: $h_1 = 1/24$, $h_\gamma = 1/9$, $h_2 = 1/47$ (the fracture mesh is coarser than the other meshes). $K_f = 2000$, $d = 0.001$. Small oscillations occur close to the fracture

zone, the permeability is $\mathbf{K}_{f,2}$, and in the other two, it is $\mathbf{K}_{f,1}$. The fourth test case concerns a “neutral fracture” in which the scalar permeability is the same as in the subdomains.

5.1 First test case: a highly permeable fracture

In this test case (see Fig. 1), the permeability K_f in the fracture is $K_f = 2000$ and thus $\mathbf{K}_\gamma = \mathbf{K}_{f,\tau}d = 2$ (see the definition of \mathbf{K}_γ following Eq. 3). Dirichlet conditions are imposed on the fracture boundaries: there is a unit pressure drop from the top of the fracture to the bottom. Thus the fluid tends to flow from right to

left and also to flow rapidly along the very permeable fracture from top to bottom. There is fluid exchange between the fracture and the rock matrix as fluid from the fracture enters the rock matrix near the top and fluid from the matrix enters the fracture near the bottom. The normal velocity is discontinuous across the fracture.

A reference computation performed with a conforming mesh is shown in Fig. 4, where we recall that the grid is considerably coarsened for visualization purposes.

A solution obtained with a nonconforming mesh is shown in Fig. 5 for the case of a highly refined fracture mesh, and in Fig. 6 for the case of a coarse fracture mesh. When the fracture mesh is coarser than the surrounding mesh, some small oscillations in the pressure and Darcy velocity can be seen in the vicinity of the fracture.

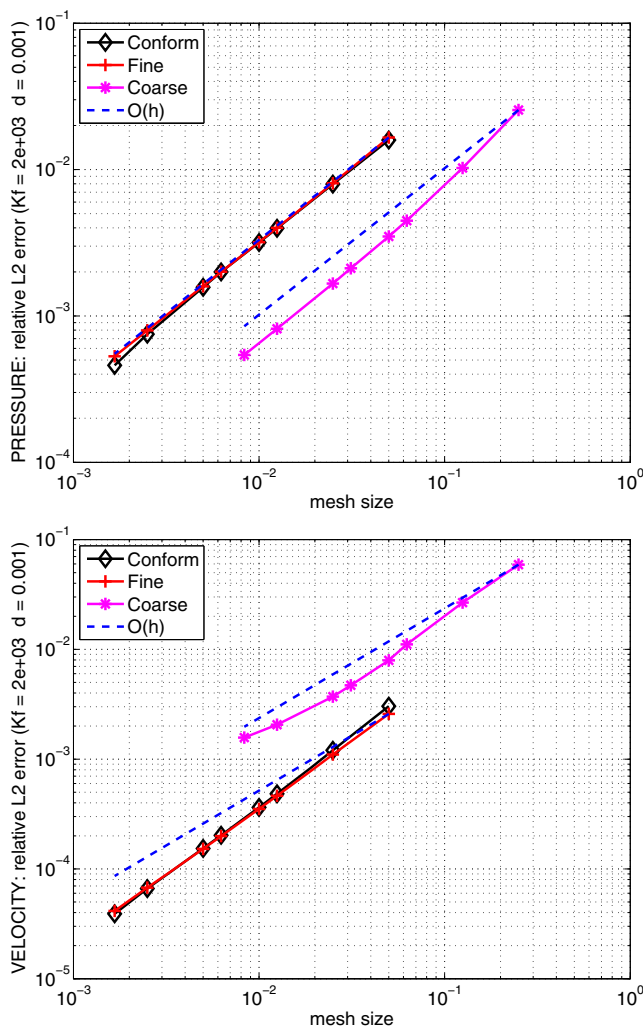


Fig. 7 Test case 1. Relative L^2 error variation as a function of the mesh size h . The three meshes are nonconforming at the interface, and the fracture is either finely (*crosses*) or coarsely (*stars*) meshed. $h_1 \approx h_2 \in [1/20, 1/600]$, and $h_\gamma \approx 0.1 h_1$ (finely meshed fracture) or $h_\gamma \approx 5 h_1$ (coarsely meshed fracture). We also report the convergence history in the conforming case (*diamonds*, $h_1 = h_2 = h_\gamma$). $K_f = 2000$, $d = 0.001$. *Top* pressure error. *Bottom* velocity error

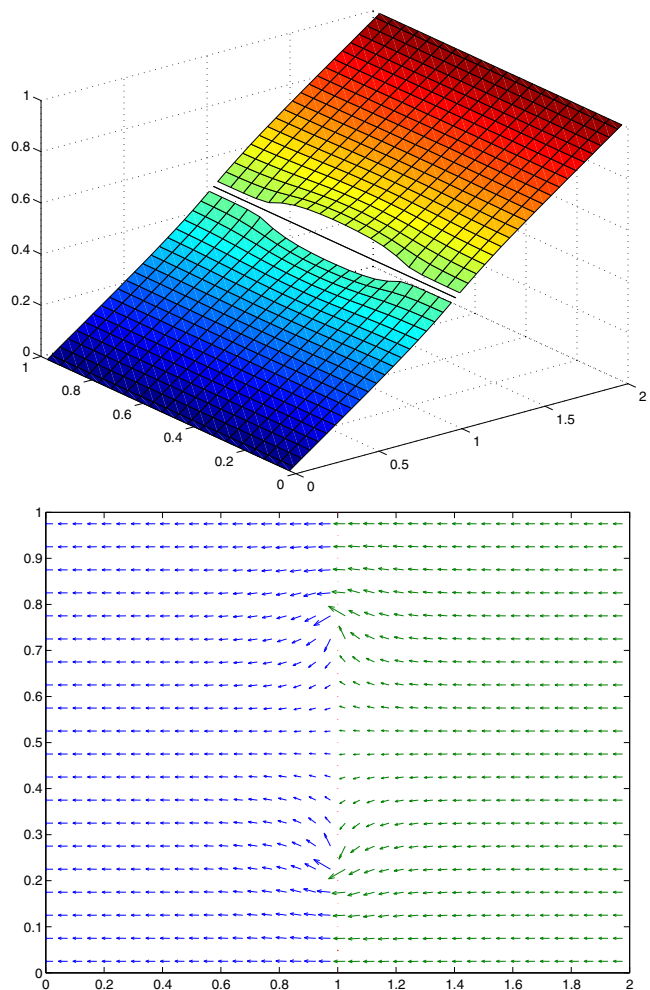


Fig. 8 Test case 2. Pressure (*top*) and Darcy velocity (*bottom*) with conforming meshes ($h_1 = h_2 = h_\gamma = 1/20$). $K_f = 0.002$, $d = 0.001$. The very small velocity can hardly be seen in the fracture

The convergence curves for the pressure and for the Darcy velocity in the L^2 norm are shown in Fig. 7 for a finely meshed fracture and for a coarsely meshed fracture. The value of h is either $1/N_{y,1}$ (in the case of a fine interface mesh) or $1/N_{y,f}^{\text{coarse}}$ (in the case of a coarse interface mesh); see Table 1. For comparison, we also show the convergence curves for conforming meshes, which are almost superimposed with the curves for the finely meshed fracture case. One obtains a linear convergence in both cases for both the pressure and for the Darcy velocity. One can even notice a slightly improved convergence rate for the Darcy velocity in the case of conforming meshes and in the case of a more finely meshed fracture.

Remark 2 In Figs. 7, 12, and 19, the error curves for the grids with the coarsely meshed fracture are shifted to

the right with respect to the curves corresponding to the grids with the finely meshed fracture or the conforming grids. This is because the h or “mesh size” of the abscissa in the case of the coarsely meshed fracture corresponds to the h of the grid on the fracture rather than the h of the more coarsely grided subdomain as in the other two cases.

5.2 Second test case: a geological barrier

In the second test case (see Fig. 2), the central half of the fracture is a barrier with $K_f = 0.002$ so that $\kappa_\gamma = 2\mathbf{K}_{f,v}/d = 4$ (see the definition of κ_γ in the paragraph following Eq. 3), while in the upper and lower quarters of the fracture, the permeability K_f is the same as in the surrounding rock matrix: $K_f = K_1 = K_2 = 1$. Homogeneous Neumann conditions are imposed at the upper

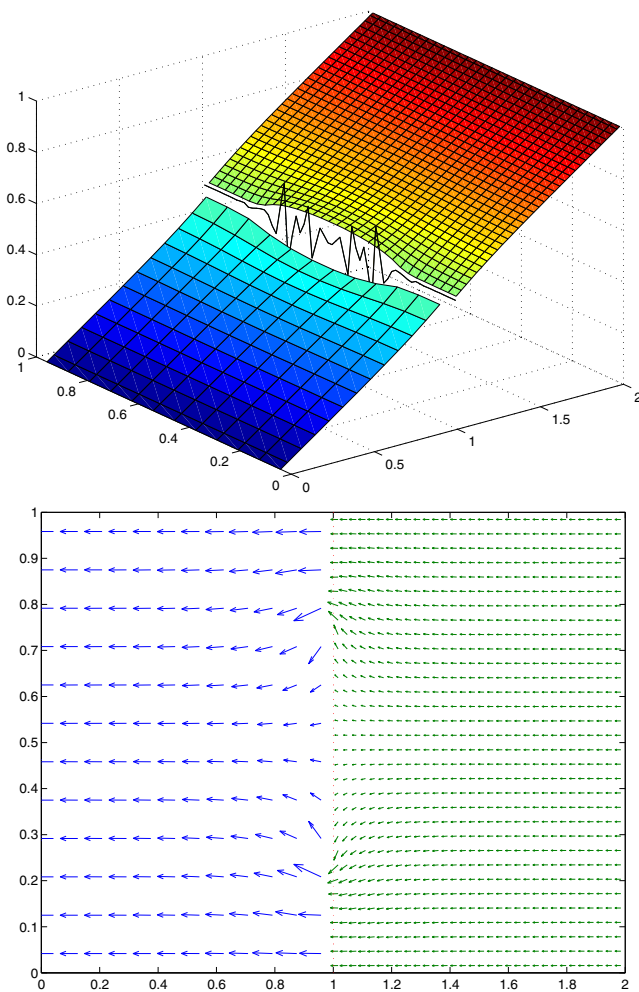


Fig. 9 Test case 2. Pressure (top) and Darcy velocity (bottom) with nonconforming meshes: $h_1 = 1/12$, $h_\gamma = 1/64$, $h_2 = 1/32$ (the fracture mesh is finer than the other meshes). $K_f = 0.002$, $d = 0.001$. The fracture pressure has large oscillations

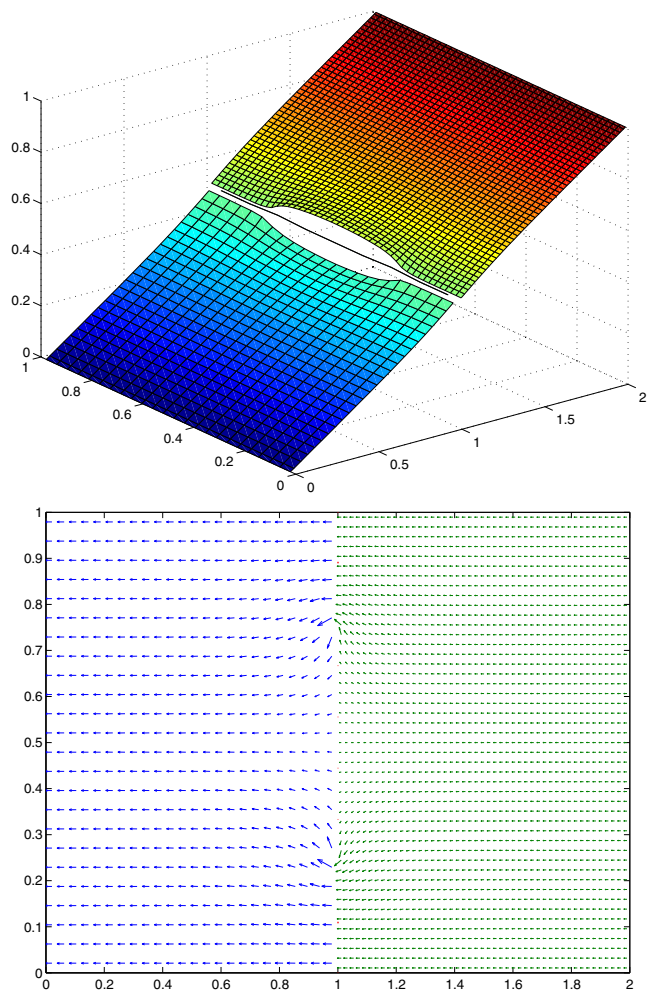


Fig. 10 Test case 2. Pressure (top) and Darcy velocity (bottom) with nonconforming meshes: $h_1 = 1/24$, $h_\gamma = 1/9$, $h_2 = 1/47$ (the fracture mesh is coarser than the other meshes). $K_f = 0.002$, $d = 0.001$

and lower boundaries of the fracture. The fluid tends to avoid the impervious fracture, and the pressure is discontinuous across the fracture. See the solution with conforming meshes in Fig. 8.

A solution obtained with a nonconforming mesh is shown in Fig. 9 for the case of a fine fracture mesh, and in Fig. 10 for the case of a coarse fracture mesh. When the fracture mesh is much finer than the surrounding mesh, some large oscillations in the fracture pressure occur. These spurious oscillations decay and cluster near the singular points when the meshes are refined while keeping the same relation between h_1 , h_2 and h_γ (cf. Figure 11).

In Fig. 12, the L^2 norm convergence curves for the pressure and for the Darcy velocity are shown for a discretization with a finely meshed fracture and with a coarsely meshed fracture. As before for comparison,

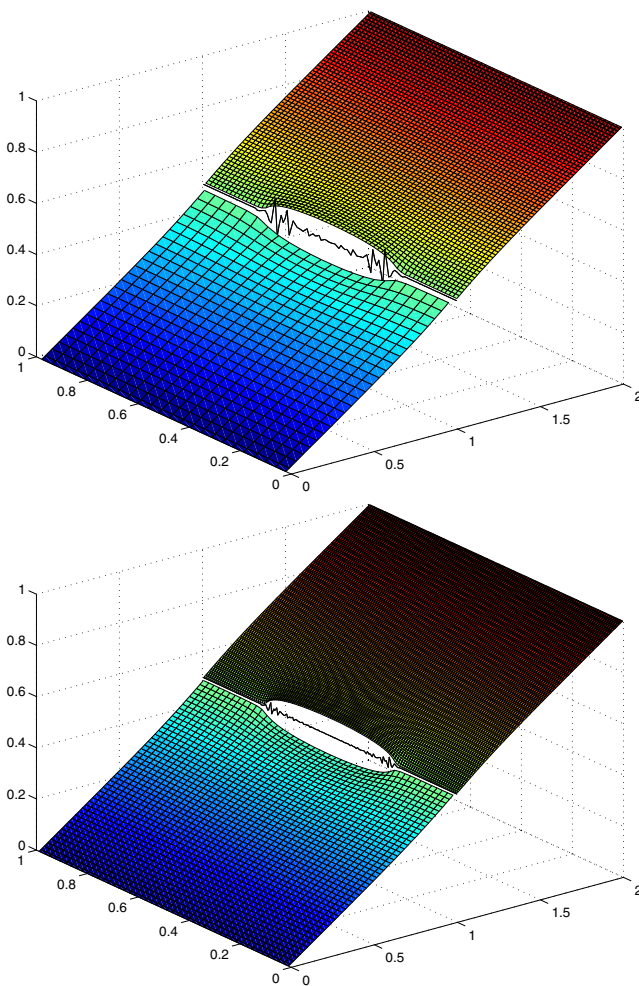


Fig. 11 Test case 2. Pressure evolution when h is refined (fine fracture case). *Top* $h_1 = 1/24$, $h_\gamma = 1/128$, $h_2 = 1/64$. *Bottom* $h_1 = 1/48$, $h_\gamma = 1/256$, $h_2 = 1/128$. $K_f = 0.002$, $d = 0.001$. The oscillations decrease with h

we also show the convergence with conforming meshes, which is very similar to that of the finely meshed case. The convergence rate for the pressure is linear as predicted theoretically. Note, however, that in both cases, the convergence of the Darcy velocity is sublinear at first ($\mathcal{O}(h^{1/2})$), before slowly reaching an asymptotic linear behavior. This behavior is also observed for conforming meshes.

We suspect that the $\mathcal{O}(h^{1/2})$ behavior of the velocity is caused by a lack of regularity of the solution at the extremities of the fracture. Indeed, let us consider the Darcy problem posed only in the Ω_2 with the same boundary conditions on the upper, lower, and righthand side boundaries as in test case 2 but with,

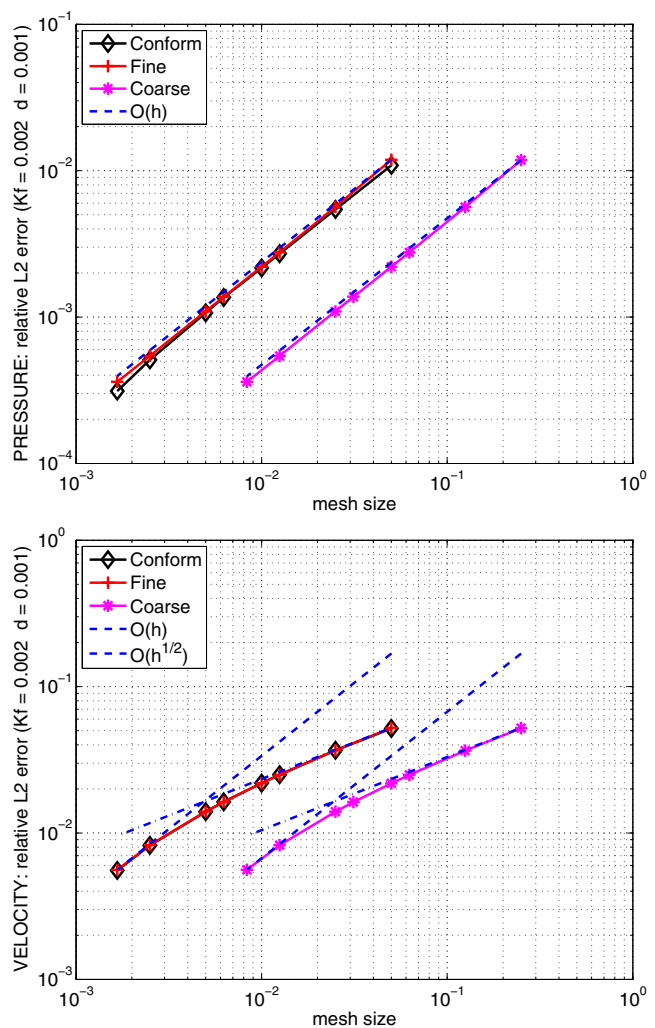


Fig. 12 Test case 2. Relative L^2 error as a function of h . The three meshes are nonconforming at the interface and the fracture is either finely (*crosses*) or coarsely (*stars*) meshed. $h_1 \approx h_2 \in [1/20, 1/600]$, and $h_\gamma \approx 0.1 h_1$ (finely meshed fracture) or $h_\gamma \approx 5 h_1$ (coarsely meshed fracture). We also report the convergence history in the conforming case (*diamonds*, $h_1 = h_2 = h_\gamma$). $K_f = 0.002$, $d = 0.001$. *Top* pressure error. *Bottom* velocity error

in place of the fracture transmission conditions on the lefthand side, the boundary condition $\mathbf{u} \cdot \mathbf{n} = 0$ for $1/4 \leq y \leq 3/4$ and $p = 0$ for $y < 1/4$ and for $3/4 < y$ (cf. Fig. 13). As the type of boundary condition changes from Neumann to Dirichlet, the solution has locally the same type of singularity as $r^{1/2} \sin(\theta/2)$ and thus

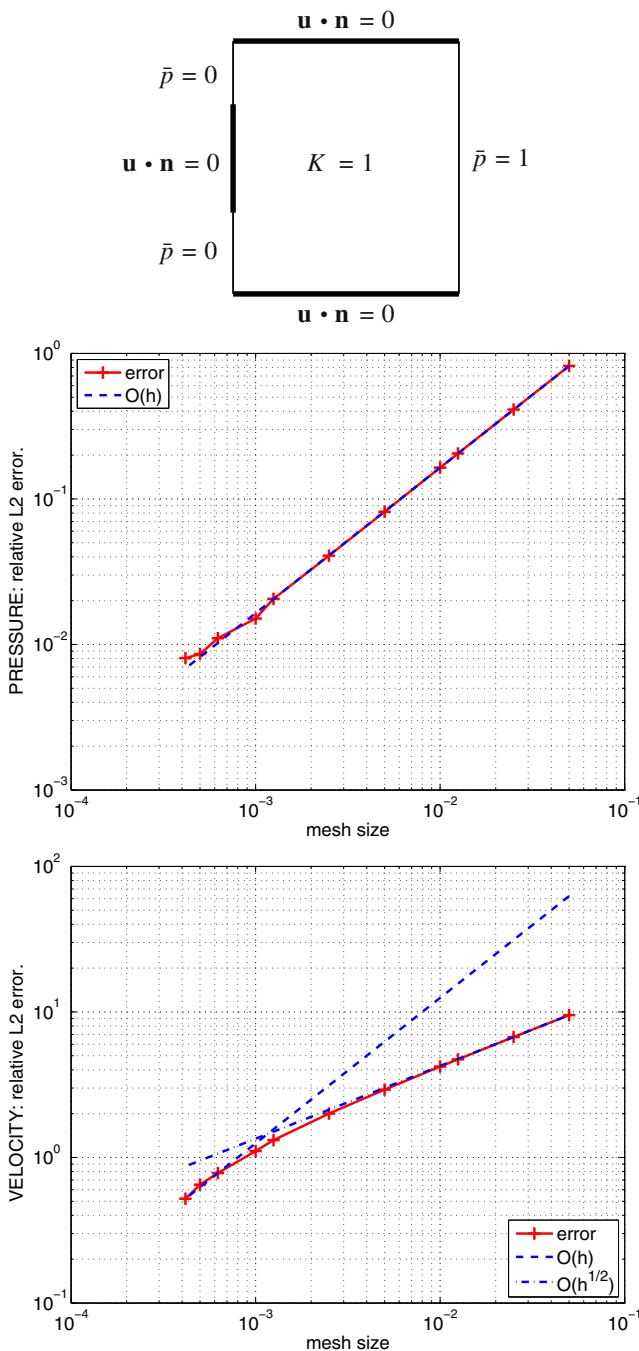


Fig. 13 Problem with less regularity. Neumann and Dirichlet boundary conditions on the lefthand side. *Top* description of the problem. *Center* convergence history in the L^2 norm of the pressure ($O(h)$). *Bottom* item for the velocity ($O(h^{1/2})$). Compare with Fig. 12

belongs to $H^{3/2-\varepsilon}(\Omega)$ for each $\varepsilon > 0$ (see [13, Theorem 2.4.3 and Corollary 2.4.4]). This is confirmed by our numerical tests (see the convergence curves for this case in Fig. 13).

Remark 3 The simple example of Fig. 13 and the fact that the convergence is identical for conforming and nonconforming meshes indicate that it is the lack of regularity that causes the suboptimal convergence of the velocity.

Finally, in Fig. 14, we show what happens when there is no fracture above and below the barrier (when $y < 1/4$ or $y > 3/4$). Instead, the continuity of p_h and $\mathbf{u}_h \cdot \mathbf{n}$ between Ω_1 and Ω_2 is weakly imposed using the mortar method, [6]. A fine mesh was used for the fracture as

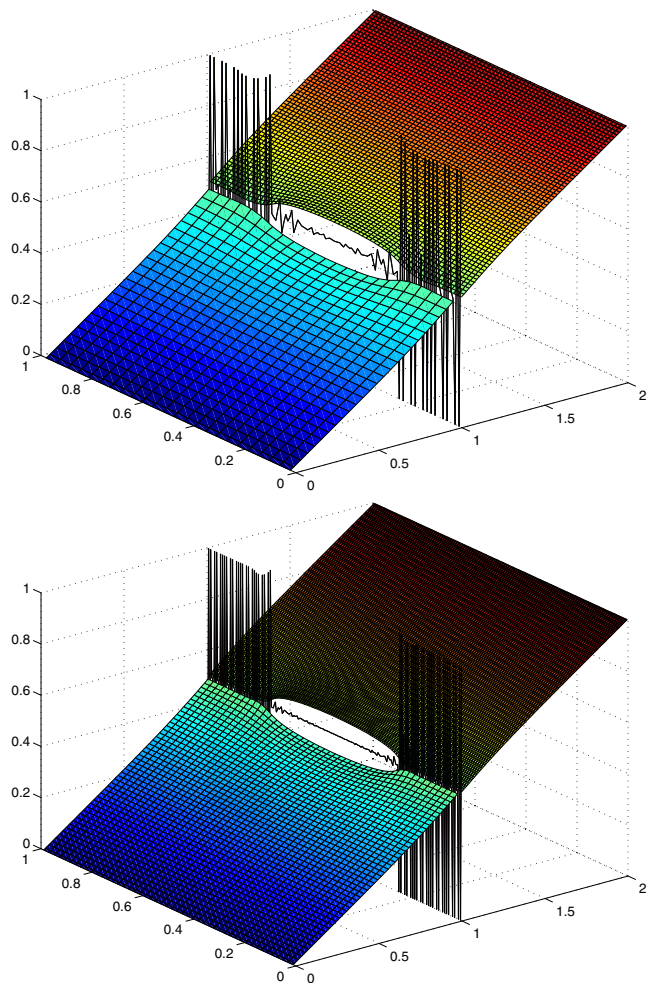


Fig. 14 Barrier in the central zone and mortar elements outside (no fracture). Pressure evolution when h is refined (fine fracture case). *Top* $h_1 = 1/24$, $h_\gamma = 1/128$, $h_2 = 1/64$. *Bottom* $h_1 = 1/48$, $h_\gamma = 1/256$, $h_2 = 1/128$. $K_f = 0.002$, $d = 0.001$. While the oscillations in the fracture decrease with h (center), the mortar oscillations do not. Compare with Fig. 11

well as for the mortars above and below the fracture. As is well known, the mortar space cannot be too rich, otherwise convergence or even solvability can be jeopardized. We clearly notice large oscillations that do not decrease with h in the mortar zone, in contrast to what occurs when there is a fracture with the same properties as the surrounding rock (see Fig. 11). This will be further explored in the example in Section 5.4.

5.3 Third test case: an anisotropic fracture

In the third test case (see Fig. 3), the fracture is heterogeneous and anisotropic, with a permeability $\mathbf{K}_{f,2}$ in the central zone and $\mathbf{K}_{f,1}$ in the other two zones:

$$\mathbf{K}_{f,1} = \begin{bmatrix} 1/k_f & 0 \\ 0 & k_f \end{bmatrix} \text{ and } \mathbf{K}_{f,2} = \begin{bmatrix} k_f & 0 \\ 0 & 1/k_f \end{bmatrix},$$

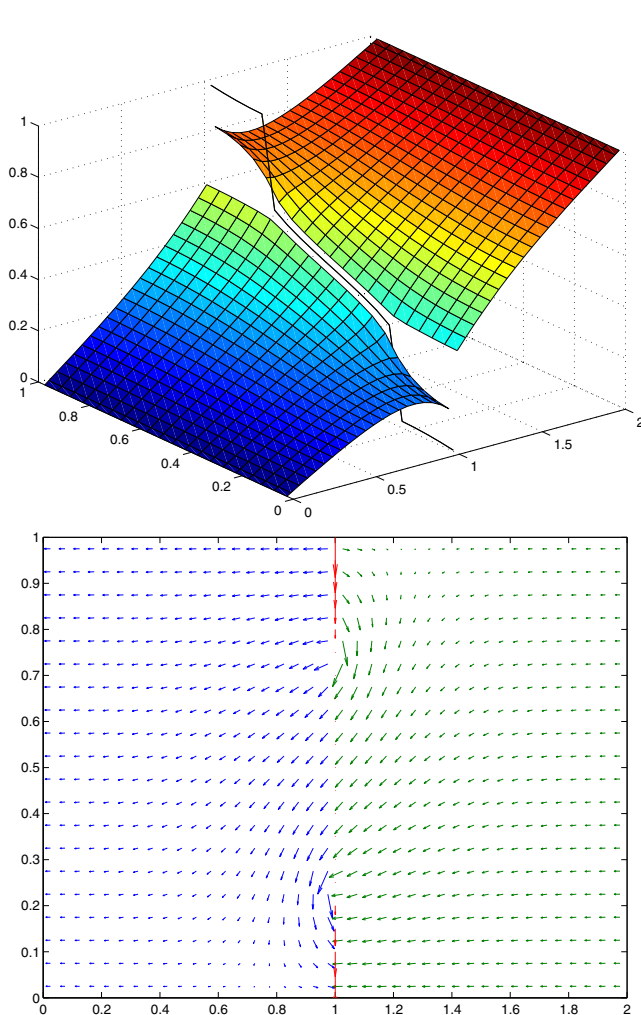


Fig. 15 Test case 3. Pressure (top) and Darcy velocity (bottom) with conforming meshes ($h_1 = h_2 = h_\gamma = 1/20$). $k_f = 2000$, $d = 0.001$. The very small velocity can hardly be seen in the central part of the fracture

where k_f is a parameter taken to be $k_f = 2000$. This means that in the central part of the fracture where the permeability is equal to $\mathbf{K}_{f,2}$, we have $K_{f,\mathbf{n}} = 2000$ and $K_{f,\tau} = 1/2000$, which implies that $\mathbf{K}_\gamma = 1/k_f d = 5 \cdot 10^{-7}$ and $\kappa_\gamma = 2k_f/d = 4 \cdot 10^6$. Thus, the fluid can hardly flow along the fracture there, but can easily cross it.

In the upper and lower quarters of the fracture, it is the opposite: $K_{f,\tau} = 2000$ and $K_{f,\mathbf{n}} = 1/2000$, which implies that $\mathbf{K}_\gamma = k_f d = 2$ and $\kappa_\gamma = 2/(k_f d) = 1$. The fluid tends to flow along the fracture, but cannot cross it.

See the solution with conforming meshes in Fig. 15. Note that both the pressure and the normal velocity are discontinuous in the upper and lower zones of the fracture, and that the solution is very irregular.

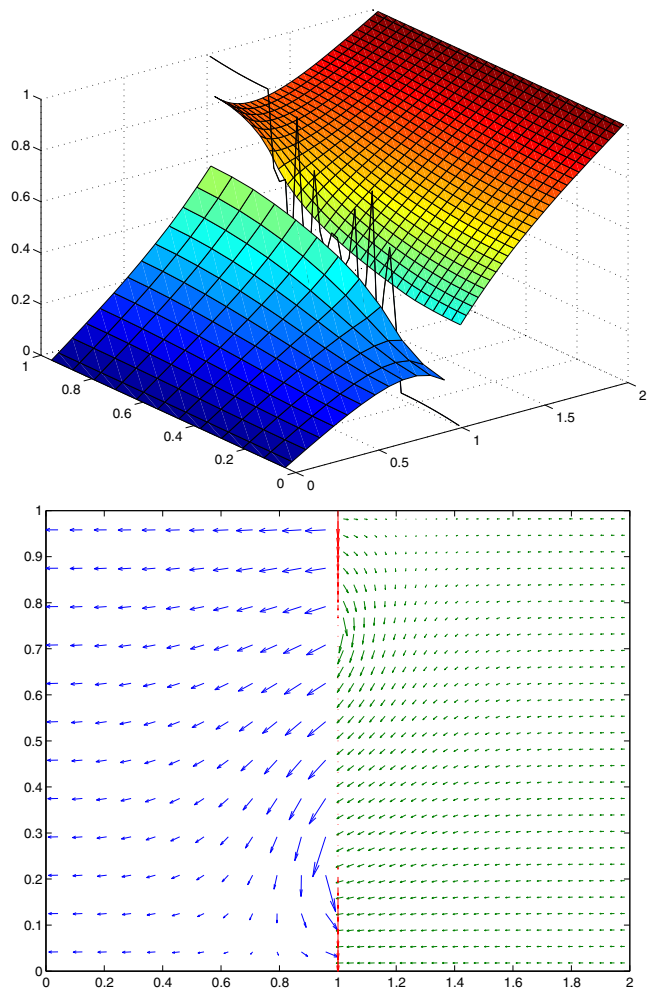


Fig. 16 Test case 3. Pressure (top) and Darcy velocity (bottom) with nonconforming meshes: $h_1 = 1/12$, $h_\gamma = 1/44$, $h_2 = 1/28$ (the fracture mesh is finer than the other meshes). $k_f = 2000$, $d = 0.001$. The fracture pressure has large oscillations in its central part

A solution obtained with a nonconforming mesh is shown in Fig. 16 in the case of a refined fracture mesh, and in Fig. 17 in the case of a coarse fracture mesh. When the fracture mesh is much finer than the surrounding mesh, some large oscillations in the fracture pressure occur, but only in the central zone where the tangential permeability is very small and the normal permeability is very large. In this central zone (almost no tangential flow, and almost no flow resistance to crossing the fracture), the effect of the fracture is very small. This is reminiscent of a mortar-type interface problem, which is known to be unstable for mortar spaces that are too rich [6]. Once again, these spurious oscillations decay slowly and cluster at the singular points, when the meshes are refined while keeping the same relation between h_1 , h_2 and h_γ (cf. Fig. 18).

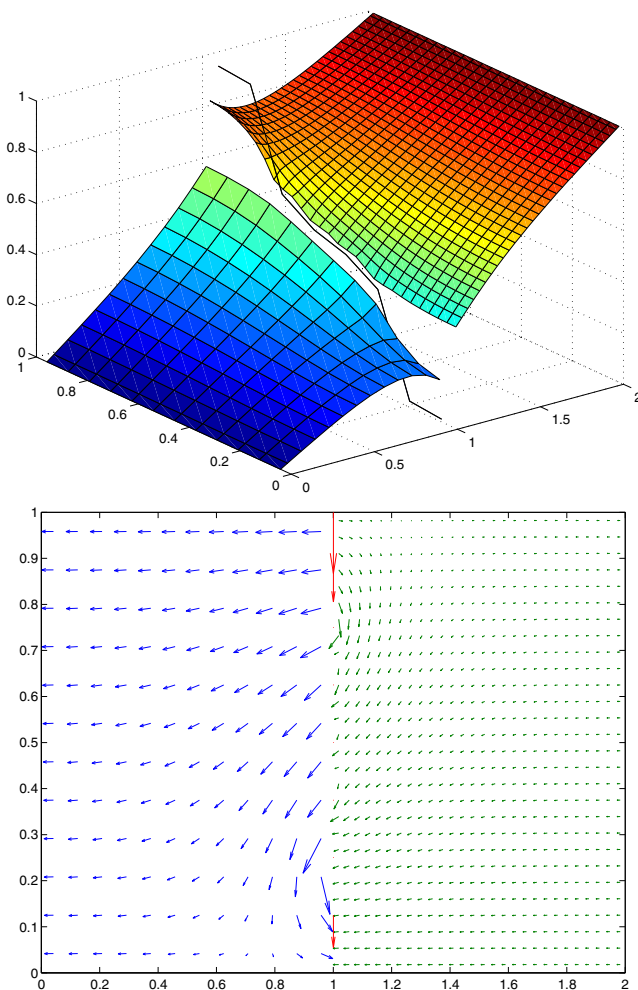


Fig. 17 Test case 3. Pressure (top) and Darcy velocity (bottom) with nonconforming meshes: $h_1 = 1/12$, $h_\gamma = 1/8$, $h_2 = 1/28$ (the fracture mesh is coarser than the other meshes). $k_f = 2000$, $d = 0.001$

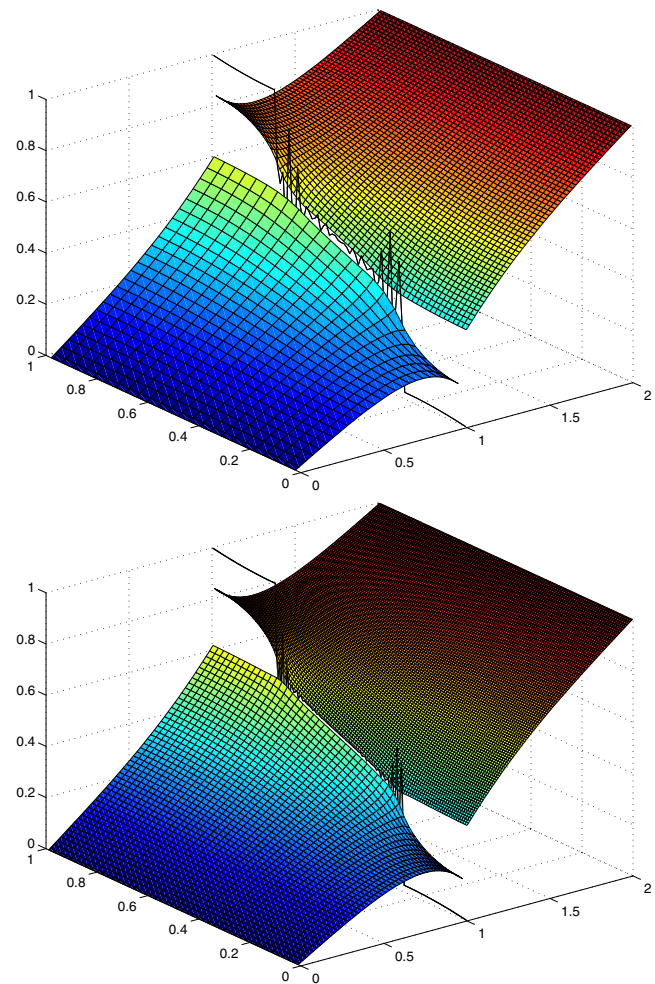


Fig. 18 Test case 3. Pressure evolution when h is refined (fine fracture case). Top $h_1 = 1/24$, $h_\gamma = 1/88$, $h_2 = 1/56$. Bottom $h_1 = 1/48$, $h_\gamma = 1/176$, $h_2 = 1/112$. $k_f = 2000$, $d = 0.001$. The oscillations decrease with h

In Fig. 19, the L^2 norm convergence curves for the pressure and for the Darcy velocity are shown for a discretization with a finely meshed fracture and with a coarsely meshed fracture. As before for comparison, we also show the convergence with conforming meshes. The convergence rate for the pressure is linear as predicted theoretically. Note, however, that in both cases, the convergence of the Darcy velocity is sublinear (between $\mathcal{O}(h^{1/2})$ and $\mathcal{O}(h)$). This behavior, due to the lack of regularity of the solution, is also observed for conforming meshes.

5.4 Fourth test case: comparison between a “neutral fracture” and a mortar interface

In this test case, we suppose that the permeability of the “fracture” is the same as that of the surrounding

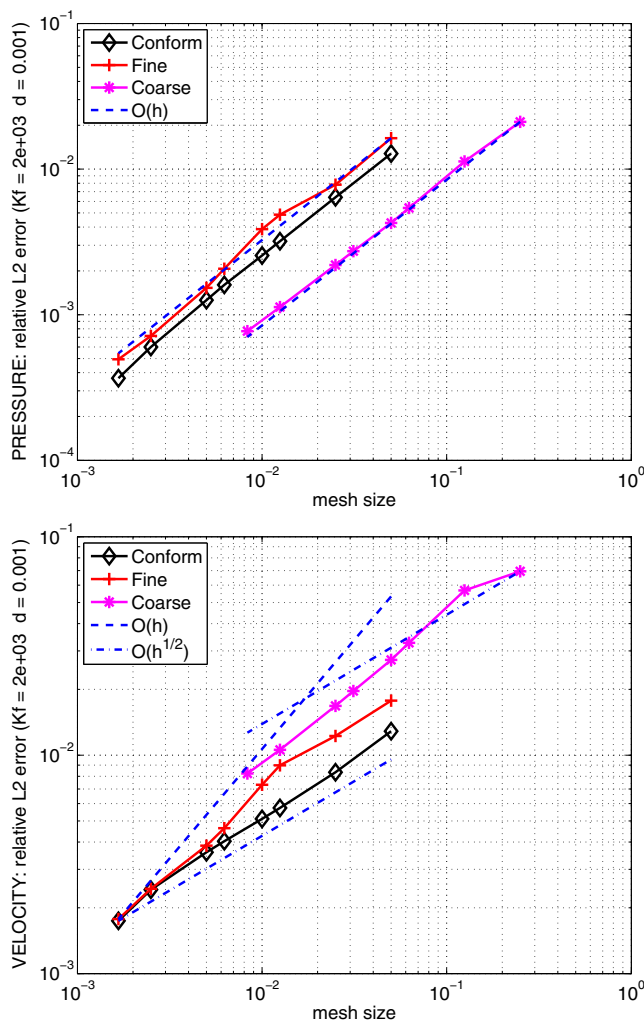


Fig. 19 Test case 3. Relative L^2 error as a function of h . The three meshes are nonconforming at the interface and the fracture is either finely (*crosses*) or coarsely (*stars*) meshed. $h_1 \approx h_2 \in [1/20, 1/600]$, and $h_\gamma \approx 0.1 h_1$ (finely meshed fracture) or $h_\gamma \approx 5 h_1$ (coarsely meshed fracture). We also report the convergence history in the conforming case (*diamonds*, $h_1 = h_2 = h_\gamma$). $k_f = 2000$, $d = 0.001$. *Top* pressure error. *Bottom* velocity error

rock matrix. No flow boundary conditions are imposed all along the top and the bottom of the domain as in test case two. There is a pressure drop from the righthand side of the domain to the lefthand side of the domain as in the other test cases; however, in order to avoid a completely one-dimensional behavior, the pressure drop is not a unit drop constant from top to bottom. On the righthand side of the domain, the pressure varies linearly from 1 at the top to 0 at the bottom, while on the lefthand side, it varies linearly from 0.2 at the top to 0 at the bottom. The permeability is $K = 1$ in both subdomains and throughout the fracture.

The purpose of this test case is to compare results obtained by two different methods for a nonconforming

grid. The first method that we call the *neutral fracture configuration* uses the scheme given in Section 4, system (5). It is simply supposed that $K_f = K_1 = K_2 = 1$. In the second called the *mortar configuration*, there is no fracture in the domain: the continuity is enforced using a mortar method as in [6] but with piecewise constant mortar elements (instead of continuous or discontinuous linear mortar elements).

The two configurations give almost identical pressures and velocities, so we show only the results obtained with the neutral fracture configuration. A solution with conforming (respectively nonconforming) meshes is shown in Fig. 20 (respectively in Fig. 21). In this subsection, the grid parameters used for the nonconforming case are given in Table 2: the second subdomain has a finer mesh, 16 squares for each square of the mesh on the first subdomain. The mesh on the fracture and the mesh on the interface for the mortar

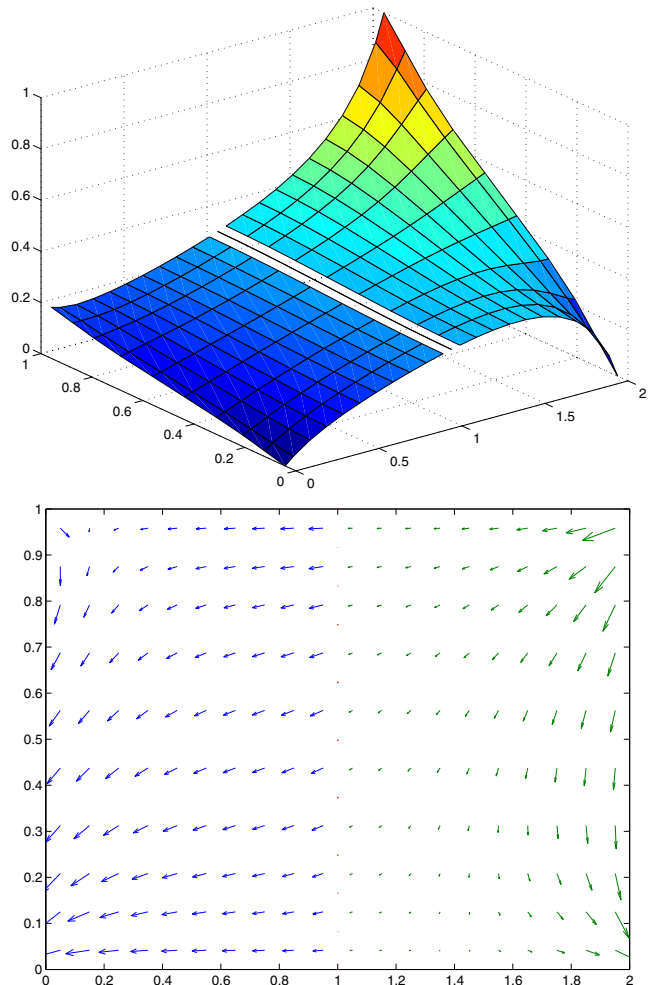


Fig. 20 Test case 4. Pressure (*top*) and Darcy velocity (*bottom*) with conforming meshes ($h_1 = h_2 = h_\gamma = 1/10$). $K_f = 1$, $d = 0.001$

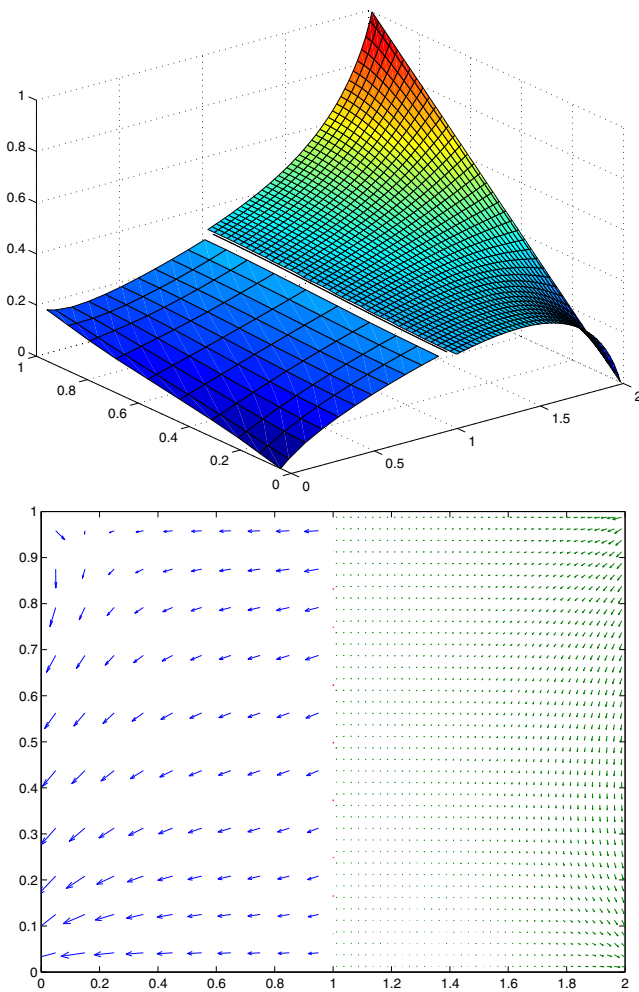


Fig. 21 Test case 4. Pressure (top) and Darcy velocity (bottom) with nonconforming meshes ($h_1 = h_\gamma = 1/10$ and $h_2 = 1/40$). $K_f = 1$, $d = 0.001$

elements are the same and coincide with the “trace” of the coarser subdomain mesh.

In Fig. 22, the L^2 norm convergence curves for the pressure and for the Darcy velocity are shown for the neutral fracture and the mortar configurations. We show the convergence with conforming and nonconforming meshes. The convergence rate for the pressure is linear as predicted theoretically. For the neutral fracture configuration, the convergence of the Darcy

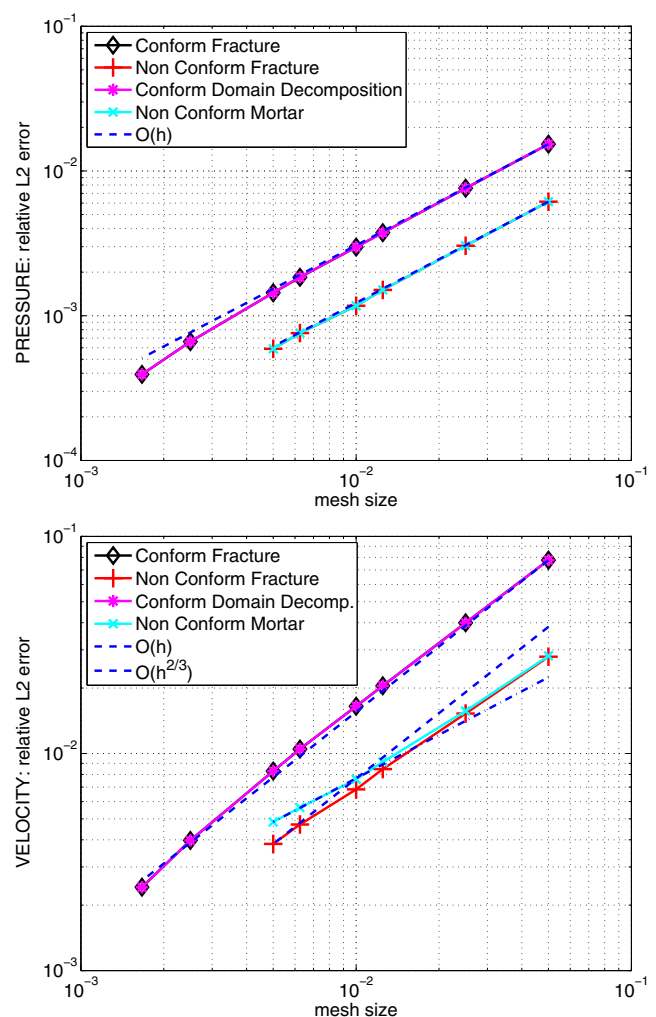


Fig. 22 Test case 4. Relative L^2 error as a function of h for the neutral fracture configuration ($K_f = 1$, $d = 0.001$) and for the mortar configuration. In both configurations, we show the convergence history in the conforming case ($h_1 = h_2 = h_\gamma \in [1/20, 1/600]$), fracture and mortar curves almost superimposed), and nonconforming case ($h_1 = h_\gamma = 4h_2 \in [1/20, 1/200]$). Top pressure error. Bottom velocity error

velocity seems to tend to the order $\mathcal{O}(h)$ as expected, whereas it is only $\mathcal{O}(h^{2/3})$ for the mortar configuration.

5.5 Conclusions concerning the numerical simulations

As expected theoretically, the L^2 convergence for the pressure is $\mathcal{O}(h)$ in all cases. The convergence of the velocity is also in good agreement with the theory, although in some cases, due to a lack of regularity of the solution, we do not obtain $\mathcal{O}(h)$ behavior.

From the limited numerical experiments shown here, the following conclusions can be drawn: when the fracture is very permeable, one should refine the fracture mesh more than the mesh in the surrounding rock, as

Table 2 Test case 4

	\mathcal{T}_1	\mathcal{T}_2	\mathcal{T}_3	\mathcal{T}_4	\mathcal{T}_5	\mathcal{T}_6
$N_{y,1}$	20	40	80	100	160	200
$N_{y,2}$	80	160	320	400	640	800
$N_{y,f}$	20	40	80	100	160	200

Number of cells (segments) on the interface from each of the two subdomain meshes and from the fracture or mortar mesh for the various mesh refinements

this both avoids small oscillations and improves the precision at the very location where the fluid flows most rapidly. When the fracture is a barrier, one should, on the contrary, use a rather coarse fracture mesh, as this avoids troublesome, possibly large oscillations in the pressure and further there is no need to have a fine discretization in a zone where almost no fluid flows. It might be useful, however, to refine at the tips of the fracture, but this has not been investigated here.

We stress that the test cases 2 and 3 were chosen to be quite severe, as they introduce very strong heterogeneities *inside* the fracture, inducing singularities. The oscillations observed for the test cases 2 and 3 are, in large part, provoked by the singular points. The suboptimal convergence behavior is independent of the nonconformity of the mesh.

6 Conclusion

In this article, we analyze, both theoretically and with numerical experiments, the effect of nonconformity of the mesh on a model for flow in a porous medium with a fracture. Contrary to what is seen when no equations are solved on the interface, as in the mortar methods [6], the fracture equations result in a “stabilizing” effect that allows for an arbitrary meshing of the fracture.

Acknowledgements The authors would like to thank the anonymous reviewers for their helpful suggestions concerning the numerical experiments and, in particular, the suggestion to include the third and fourth test cases.

References

- Alauzet, F., Mehrenberger, M.: \mathbf{P}^1 -conservative solution interpolation on unstructured triangular meshes. *Int. J. Numer. Methods Eng.* **84**(13), 1552–1588 (2010)
- Alboin, C., Jaffré, J., Roberts, J.E., Serres, C.: Modeling fractures as interfaces for flow and transport in porous media. In: Chen, Z., Ewing, R.E. (eds.) *Fluid flow and transport in porous media: mathematical and numerical treatment* (South Hadley, MA, 2001), number 295 in *Contemp. Math.*, pp 13–24. Amer. Math. Soc. Providence, RI USA (2002)
- Alboin, C., Jaffré, J., Roberts, J.E., Serres, C.: Domain decomposition for flow in porous fractured media. In: Lai, C.-H., Bjorstad, P.E., Cross, M., Widlund, O.B. (eds.) *Domain Decomposition Methods in Sciences and Engineering*, pp. 365–373. Domain Decomposition 1999)
- Amir, L., Kern, M., Martin, V., Roberts, J.E.: Décomposition de domaine pour un milieu poreux fracturé: un modèle en 3d avec fractures qui s'intersectent. *ARIMA* **5**, 11–25 (2006)
- Angot, Ph., Boyer, F., Hubert, F.: Asymptotic and numerical modelling of flows in fractured porous media. *M2AN* **43**(2), 239–275 (2009)
- Arbogast, T., Cowsar, L.C., Wheeler, M.F., Yotov, I.: Mixed finite element methods on non-matching multiblock grids. *SIAM J. Numer. Anal.* **37**, 1295–1315 (2000)
- Bernardi, C., Maday, Y., Patera, A.T.: A new nonconforming approach to domain decomposition: the mortar element method. In: *Nonlinear partial differential equations and their applications. Collège de France Seminar, vol. XI* (Paris, 1989–1991). Pitman Res. Notes Math. Ser., vol. 299, pp 13–51. Longman Sci. Tech., Harlow (1994)
- Brezzi, F., Fortin, M.: *Mixed and Hybrid Finite Element Methods*. Springer, Berlin (1991)
- D'Angelo, C., Scotti, A.: A mixed finite element method for Darcy flow in fractured porous media with non-matching grids. *Math Model Numer Anal* **46**(02), 465–489 (2012)
- Faille, I., Flauraud, E., Nataf, F., Pegaz-Fiornet, S., Schneider, F., Willien, F.: A new fault model in geological basin modelling, application to finite volume scheme and domain decomposition methods. In: Herbin, R., Kroner, D. (eds.) *Finite volumes for complex applications III*, pp. 543–550. Hermès Penton Sci. (2002)
- Frih, N., Roberts, J.E., Saada, A.: Un modèle Darcy-Forchheimer pour un écoulement dans un milieu poreux fracturé. *ARIMA* **5**, 129–143 (2006)
- Frih, N., Roberts, J.E., Saada, A.: Modeling fractures as interfaces: a model for Forchheimer fractures. *Comput. Geosci.* **12**, 91–104 (2008)
- Grisvard, P.: *Singularities in Boundary Value Problems. Recherches en Mathématiques Appliquées [Research in Applied Mathematics]*, vol. 22. Masson, Paris (1992)
- Huang, H., Long, T., Wan, J., Brown, W.: On the use of enriched finite element method to model subsurface features in porous media flow problems. *Comput. Geosci.* **15**, 721–736 (2011). doi:[10.1007/s10596-011-9239-1](https://doi.org/10.1007/s10596-011-9239-1)
- Jaffré, J., Martin, V., Roberts, J.E.: Generalized cell-centered finite volume methods for flow in porous media with faults. In: *Finite Volumes for Complex Applications, III*, pp. 343–350. Hermes Sci., Paris (2002)
- Lessingo, M., D'Angelo, C., Quarteroni, A.: A multiscale Darcy–Brinkman model for fluid flow in fractured porous media. *Numer. Math.* **117**(4), 717–752 (2011)
- Martin, V., Jaffré, J., Roberts, J.E.: Modeling fractures and barriers as interfaces for flow in porous media. *SIAM J. Sci. Comput.* **26**(5), 1667–1691 (2005)
- Moreles, F., Showalter, R.E.: The narrow fracture approximation by channeled flow. *J Math Anal Appl* **365**(1), 320–331 (2010)
- Reichenberger, V., Jakobs, H., Bastian, P., Helmig, R.: A mixed-dimensional finite volume method for multiphase flow in fractured porous media. *Adv. Water Resour.* **29**(7), 1020–1036 (2006)
- Roberts, J.E., Thomas, J.-M.: Mixed and hybrid methods. In: Ciarlet, P.G., Lyons, J.-L. (eds.) *Handbook of Numerical Analysis*, vol. 2, pp. 523–639. Elsevier, Amsterdam (1991)
- Tunc, X., Faille, I., Gallouët, T., Cacas, M., Havé, P.: A model for conductive faults with non-matching grids. *Comput. Geosci.* **16**(2), 277–296 (2012) doi:[10.1007/s10596-011-9267-x](https://doi.org/10.1007/s10596-011-9267-x)